Design and characteristics of a cavity-enhanced Fourier-transform spectrometer based on a supercontinuum source

A. Libert,[1] X. Urbain,[1] B. Fabre,[2] M. Daman,[1] and C. Lauzin[1, a)]
[1)]*Institute of Condensed Matter and Nanosciences, Université catholique de Louvain, B-1348 Louvain-la-Neuve, Belgium*
[2)]*Université de Bordeaux, CNRS, CEA, CELIA, UMR5107, F33405 Talence, France*

(Dated: 22 September 2020)

We report the in-house fabrication of a high resolution Fourier transform spectrometer (FTS) for the spectroscopy of molecules in the gas phase at resolutions down to 0.002 cm^{-1} working in the spectral range from 5880 cm^{-1} (1.7 μm) to 15380 cm^{-1} (650 nm). The FTS employs a supercontinuum as a broadband light source and a He:Ne laser with a homemade frequency-stabilization scheme as the spatial reference for the sampling of the interferogram on a constant optical path difference (OPD) grid. The sampling of the two lasers is performed at constant time intervals and the resampling process is performed at the software level. The resampling of the interferogram on a constant OPD grid relies on cubic approximations of the He:Ne interference pattern to determine its zero-crossings. The use of an invariant in the sampling process allows to perform on-the-fly data treatment. Both the hardware aspect and the data processing are described with, in each case, an original approach. We also report the successful coupling of the FTS with a high finesse optical cavity with effective mirror reflectivities of 99.76%, allowing to reach sensitivities down to 6.5×10^{-8} cm^{-1} with a RMS accuracy of 0.0017 cm^{-1} on the position of the Doppler-broadened transitions with a mean transition width of 0.046 cm^{-1} for spectra recorded at a spectral resolution of 0.015 cm^{-1}. The sensitivity of the instrument per spectral element, once normalized, represents the best sensitivity reported in the literature for Fourier-transform incoherent broadband cavity-enhanced absorption spectroscopy with a supercontinuum light source.

I. INTRODUCTION

From fundamental physics to the industrial world and environmental monitoring, optical spectroscopy is an invaluable tool, allowing for the quantitative analysis and identification of molecules via their unique spectral fingerprints. For example, trace detection of some impurities in the semi-conductor manufacturing gives tremendous information about the quality of the end products[1]. In the case of environmental monitoring, optical spectroscopy allows for the detection and quantification of some greenhouse gases and pollutants, such as carbon dioxide, methane and formaldehyde.

The ideal instrument to perform optical spectroscopy should be broadband, sensitive and it should also have a sufficiently high resolution to observe the ro-vibrational signature of molecules, all this ideally in a short acquisition time.

There are numerous measuring techniques that can be used to perform optical spectroscopy but they usually do not embody all these features and some compromise has to be made when selecting a technique for a given application. While techniques such as continuous wave absorption spectroscopy and cavity ring-down spectroscopy permit sensitive measurements at high resolution, they suffer from their inability to cover broad spectral ranges in a modest amount of time[2]. Broadband cavity-enhanced absorption spectroscopy tackles this drawback but it requires the ability to measure the irradiance spectrum of a source of light after its transmission through the optical cavity[3]. However, this measurement cannot be performed in a direct manner, by placing a photodetector in front of the incoming radiation and recording its intensity with respect to time in order to take its Fourier-transform. Indeed, there is no detector and no electronics fast enough to respond to optical frequencies (about several hundreds of THz) which are about 5 orders of magnitude higher than the fastest detectors[4]. There are three common approaches to overcome this difficulty and resolve light with regard to its frequency, (1) only the light intensity in the spectral range of interest is measured thanks to the use of optical filters, (2) the spectral components of the light source are spatially separated with the help of dispersive instruments like gratings or prisms and their intensities measured with distinct detectors, (3) the interference signal at the output of a Michelson interferometer is recorded at specific values of optical path difference (OPD) induced in one of the arms of the interferometer. This signal is known as the interferogram. The spectrum is retrieved from the interferogram by means of the mathematical Fourier transform. This last approach is at the root of Fourier-transform spectrometry.

Fourier transform spectrometers (FTS) present three main advantages over the dispersive- and filter-based approaches. Firstly, all the frequencies are recorded at the same time on a single photodetector. The contribution of each of these frequencies to the signal is then determined by taking the Fourier transform of this signal. This is known as the multiplex advantage or Felgett's advantage[5]. Secondly, light throughput for a given resolution is superior to the two other aforementioned techniques, allowing for higher signal-to-noise ratio measurements in a given amount of time compared to dispersive- and filter-based approaches. This is known as Jacquinot's advantage[6]. Finally, the frequency scale of the spectrum is obtained via a reference laser in Fourier transform spectrometers, leading to self-calibrated spectra. This feature is Connes'advantage of FTS[7].

[a)]Electronic mail: Authors to whom correspondence should be addressed clement.lauzin@uclouvain.be and alexis.libert@uclouvain.be

Since the apparition of the first commercial rapid scanning FTS in 1969[8], lots of progress were made in the design and the development of these instruments. They are now a mature technology and commercial FTS with resolution down to 0.0009 cm^{-1} are commercially available and used in laboratories all over the world, making them one of the workhorses of high-resolution molecular spectroscopy. They usually rely on conventional thermal sources to perform spectroscopy. In order to improve their sensitivity, the optical path through the sample must be increased. This is usually accomplished by using multi-pass cells but this approach suffers from the requirement of large sample volumes to reach interaction lengths of several hundreds of meters and an ill-defined interaction region. Another approach relies on the use of optical cavities instead of multi-pass cells, reducing by more than two orders of magnitude the volume required for a similar interaction length. The use of an optical cavity, along with an incoherent broadband light source and a FTS allows a considerable improvement in the sensitivity of the measurement while preserving the high resolution and the broadband characteristics of FTS. This combination was first reported by Ruth *et al.*[9] where a 75W Xe arc-lamp was successfully coupled to a cavity and a commercial FTS. This technique was named *Fourier-transform incoherent broadband cavity-enhanced absorption spectroscopy* or FT-IBBCEAS. Unfortunately, optical cavities exclude the use of thermal light sources because of the very poor coupling throughput due to their spatial divergence and low spectral brightness[10]. Alternative light sources for FT-IBBCEAS are light emitting diodes and supercontinuum light sources. Supercontinuum light sources have the ability to produce several watts of pulsed radiation on a very broad spectral range in the visible and infrared domains. Furthermore, the emitted light is already collimated, facilitating its coupling with optical cavities. Two groups made use of these light sources in FT-IBBCEAS setups[11,12].

This article presents the design and fabrication of a Fourier transform spectrometer for high resolution spectroscopy, with resolution down to 0.002 cm^{-1}. Measurements are performed in an auto-balanced detection scheme and acquisition is performed at constant time intervals. Resampling of the interferograms on an uniform OPD grid is performed at the software level. The instrument is capable of covering the spectral range from 5900 cm^{-1} to 14300 cm^{-1} by employing a supercontinuum laser source as the broadband source.

Motivations for building from scratch a FTS for high-resolution molecular spectroscopy were multiple. Two broadband light sources were available in the laboratory: a MIRA900 femtosecond laser from Coherent and a SC450-4 supercontinuum from Fianium, but there was no instrument to perform spectroscopy with them. Also, building an instrument makes it highly customisable and gives us a complete understanding of its assets and limitations. Finally, it allows us to implement the new paradigms relying on the use of frequency-stabilized frequency combs in Fourier transform spectroscopy that appeared in the last few years. These paradigms allow to extend the range of applications of Fourier-transform spectroscopy to metrological applications[13] while suppressing the instrumental lineshape function due to the finite length of the translation stage that induces the OPD in the instrument and even to surpass the maximum resolution of conventional FTS[14,15]. Their implementation requires a complete control on the data processing pipeline of the FTS which can only be achieved by means of a customized software. Furthermore, combining a FTS with a frequency comb coupled to an optical cavity requires the ability to record the two outputs of the interferometer because of the frequency-to-amplitude noise conversion resulting from their coupling.

Surprisingly, while there is a renewed interest in building or refurbishing in-house FTS for either economical or customization purposes[3,16,17] and even if numerous articles discuss specific parts of the design of FTS, we did not find any article in the literature describing the complete design and development of such an instrument, including both the software and hardware aspects. Also, with the progress concerning, amongst others, computational power and data acquisition, alternative approaches compared to commercial instruments were considered in this work. These approaches make feasible the fabrication of high resolution FTS with limited material and human resources. The goal of this article is to fill the gap in the literature by precisely describing our instrument, presenting the advantages and limitations of our design and discussing some aspects and choices that were made during the development process for other groups to build their own high resolution FTS and gain a significant amount of time.

In this article, we will assume the reader is familiar with Fourier transform spectrometers and the principles behind these instruments. A description of their working principle can be found in Ref.[4,18,19]. To facilitate the discussion, some of these concepts are briefly reintroduced in section II.

Section III describes the hardware of the instrument in its current form. Section IV concerns the data processing pipeline which is at the heart of the instrument. Section V describes the performances of our instrument in terms of its instrumental lineshape function, its wavenumber accuracy and sensitivity. Furthermore, the instrument is benchmarked against the setup of O'Leary *et al.*[12]. Indeed these authors performed FT-IBBCEAS while having many features in common but they rely on a commercial Bruker FTS.

II. WORKING PRINCIPLE

Fourier transform spectrometers rely on the use of a Michelson interferometer to measure the light spectrum. When injecting a monochromatic light source in this kind of interferometer, light undergoes constructive or destructive interference depending on the relative distance travelled by the beam in the two arms of the interferometer, resulting in a sine-squared interference pattern at its output with respect to the OPD. Since the light source employed for spectroscopy covers a large spectral range, its spectral components will undergo constructive or destructive interference for different OPDs. Intensity at the detector for a given OPD $I(\delta)$ is the sum of the interference patterns of all the spectral components, that

is :

$$I(\delta) = \int_0^{+\infty} B(\tilde{\nu}) \cos(2\pi\tilde{\nu}\delta)\, \mathrm{d}\tilde{\nu}, \tag{1}$$

where $\tilde{\nu}$ is the wavenumber and $B(\tilde{\nu})$ is the spectral irradiance which is the quantity of interest. $I(\delta)$ is the measured quantity and it is named interferogram. The spectral irradiance is obtained by taking its cosine transform :

$$B(\tilde{\nu}) = \int_0^{+\infty} I(\delta) \cos(2\pi\tilde{\nu}\delta)\, \mathrm{d}\delta. \tag{2}$$

In this expression, only the positive OPDs are considered. The interferogram is said to be single-sided. Theoretically, the interferogram is an even function of the OPD, *i.e.* $I(\delta) = I(-\delta)$, and taking double-sided interferograms, that is interferograms measured on a symmetrical range of retardation around the zero path difference (ZPD), *i.e.* $\delta = 0$, is unnecessary. However, the measurement of single-sided interferograms makes the instrument sensitive to phase errors, as detailed in section IV. Information about the phase is retrieved by replacing the cosine transform by a Fourier transform in equation (2), leading to :

$$B(\tilde{\nu}) = \frac{1}{2} \int_{-\infty}^{+\infty} I(\delta) \mathrm{e}^{2\pi \mathrm{j}\tilde{\nu}\delta} \mathrm{d}\delta. \tag{3}$$

with j the imaginary number. This equation means that the irradiance spectrum can be retrieved from the knowledge of the double-sided interferogram using a Fourier transform, the two conjugate variables being the OPD and the wavenumbers. The Fourier transform is evaluated using the fast Fourier transform (FFT) algorithm, implying to know the interferogram on an uniform OPD grid. This uniform OPD grid is determined using the interference pattern of a frequency-stabilized laser as the spatial reference.

III. DESIGN OF THE INTERFEROMETER

A schematic of the optical bench in its current configuration is presented in Figure 1. The layout with both retroreflectors placed back-to-back on the moving carriage is adapted from Refs.[3,16,20,21]. Such a layout presents the advantages of compactness and of a higher opto-mechanical gain, *i.e.* the OPD induced by the carriage displacement is multiplied by four with respect to the distance travelled by the carriage instead of two as in most FTS. Also, the optical contact, that is the position of the carriage such that both arms of the interferogram are equal in length, is located at the centre of the translation stage, allowing the measurement of double-sided interferograms. The translation stage is 1.5 meters long (limited to 1.35 meters for practical purpose), leading to an ultimate spectral resolution of 0.002 cm^{-1} for the FTS. All the optics, except the high-reflectivity mirrors of the optical cavity and the beamsplitter, are standard optics from the Thorlabs catalog. The beamsplitter is the only optical element especially designed for the application and consists of a VIS/Q IT501/2 beamsplitter of Bruker. For the moment, the instrument is exposed to ambient air, restricting the spectral range of the instrument to regions where neither water, oxygen nor carbon dioxide present strong absorption. This represents one of the limitations of the current design.

Frequency-stabilized He:Ne reference laser

The purpose of the reference laser in the FTS is two-fold : it serves as a spatial reference for the resampling of the broadband source and it is utilized for the proper alignment of the instrument. The use of a laser as a spatial reference implies that its wavelength should remain constant during the whole measurement session.

The reference laser is an unpolarized He:Ne laser (model GLG5002 of NEC, manufactured in 1981). It was frequency-stabilized in-house by stabilizing its cavity length. The error signal is obtained by measuring the difference in intensity of the two orthogonally-polarized modes that can be sustained in the gain curve of the laser. We impose this difference to be equal to zero. These two modes are spatially separated by means of a polarizing beamsplitter and their intensity measured with two photodiodes. This approach is described, amongst others, in Refs.[22,23]. The cavity length is then adjusted by heating up or cooling down a piece of copper surrounding the discharge tube using thermoelectric coolers. This approach was also chosen by Shirvani *et al.*[24]. The controller used to fulfil the task is the PID controller Max 1978 from Maxim. Frequency stability of the laser was determined by injecting two identical stabilized He:Ne lasers in a temperature-stabilized Fabry-Perot interferometer, with a free spectral range (FSR) of 1GHz (FPI100 of Toptica) and by monitoring the fluctuations in relative positions x and y of the two He:Ne lasers during the length sweep of the Fabry-Perot interferometer, as shown in Figure 2 using the following formula :

$$\Delta\nu = \frac{y-x}{z} * 1\ \mathrm{GHz} \tag{4}$$

where $\Delta\nu$ is the frequency difference between the two lasers. Conversion in units of frequency relies on the knowledge of the FSR of the Fabry-Perot interferometer. Variations of $\Delta\nu$ with respect to time indicate a frequency drift of one laser with respect to the other. Fluctuations inferior to 3 MHz over a 45 minutes period of time were observed with this method, meaning that the wavelength varied by less than 4 fm during this period. Similar results were obtained by observing the beating of the two frequency stabilized He:Ne lasers.

In order to use the He:Ne laser as a reference for the retrieval of the constant OPD grid, it is also important to have a constant contrast over the complete travel of the translation stage. Requirements on (1) the polarization of the He:Ne laser, (2) its divergence and (3) its frequency stability should be fulfilled to ensure the constant contrast. For (1), a linear polarizer is directly placed at the output of the He:Ne laser to suppress one of the two orthogonal modes emitted by the laser. Otherwise, a modulation is observed in the envelope of the He:Ne

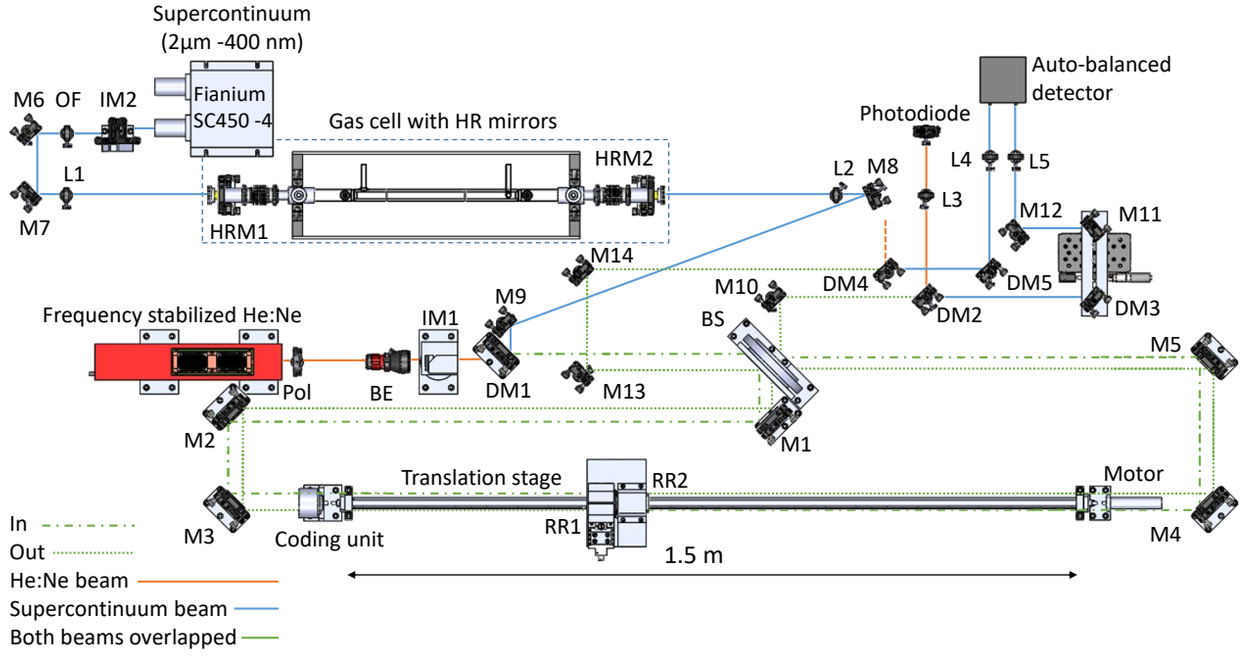

FIG. 1. Layout of the Fourier transform spectrometer with the illustration of the path of the different light beams. BE : beam expander, DM : dichroic mirror, HRM : high reflectivity mirror, IM : injection mirror, L : lens, M : mirror, OF : optical filter, RR : retroreflector. Mirrors M1, M2, M3, M4 and M5 are 2-inch silver mirrors (Ref. PF20-03-P01 from Thorlabs). The other mirrors are 1-inch silver mirrors (Ref. PF10-03-P01 from Thorlabs). The retroreflectors are 2-inch corner cubes that rely on total internal reflection (Ref. PS976M from Thorlabs). The 2-inch dichroic mirror DM1 (Ref. DMLP650L from Thorlabs) and the 1-inch dichroic mirrors DM3 and DM5 (Ref. DMLP650 from Thorlabs) are transparent for wavelengths smaller than 650 nm and reflective for wavelengths from 650 nm to 1600 nm. The 1-inch dichroic mirrors DM2 and DM4 (Ref. DMSP650 from Thorlabs) are reflective for wavelengths smaller than 650 nm and transparent for wavelengths from 650 nm to 1600 nm.

interference pattern. For (2), a beam expander is employed to enlarge the spot size in order to reduce the beam divergence and to ensure a constant spot size at the output of the interferometer. The beam expander is tuned by imposing the spots issuing from the two arms of the interferometer to have the same diameter when the carriage is in the vicinity of the optical contact. Finally, for (3), the reference laser should have a coherence length longer than the maximum OPD that can be induced by the translation stage. In our case, considering fluctuations in frequency of 3 MHz for the laser light source, we have a coherence length of about 100 meters, more than 30 times the maximum OPD.

As already mentioned, the He:Ne laser is also employed for alignment purposes. A correct alignment of the instrument is mandatory to obtain good quality spectra at high resolution in a modest amount of time. Indeed, the beams coming from the two arms of the interferometer should perfectly overlap at the detector for any position of the translation stage described in a following section. The He:Ne laser beam is first injected parallel to the translation stage by imposing it to pass through two iris diaphragms located between the beamsplitter BS and mirror M5. Two other diaphragms located between mirrors M1 and M2 allow for the alignment of the beamsplitter BS and mirror M1. The four mirrors M2, M3, M4 and M5 are aligned thanks to a circular aperture placed instead of the two retroreflectors on the carriage. Two mirrors, one on each side of the translation stage, are aligned when the carriage is at one extreme position, near the coding unit, while the two others are aligned when the carriage is at the other extreme position, near the DC motor. Alignment is considered to be fine when light is retro-injected into the laser. This can be checked by looking at the error signal of the He:Ne laser which becomes erratic when it is the case. The retroreflectors are then placed on the carriage and one of the retroreflectors is translated with respect to the other to maximize the contrast of the He:Ne interference pattern. After proper alignment, the fringe visibility smoothly varies between 0.85 and 0.91 on the complete course of the carriage, with a mean value of 0.88 for a He:Ne laser beam with a 5mm diameter at the output of the beam expander ($1/e^2$ criterion).

Once the FTS is aligned for the reference laser, injection of the broadband light source in the instrument is straightforward. Its beam is overlapped to the He:Ne laser beam using the dichroic mirror DM1. It has to pass through the same two iris diaphragms located between the beamsplitter BS and mirror M5. The two beams are separated at the output using dichroic mirrors as well.

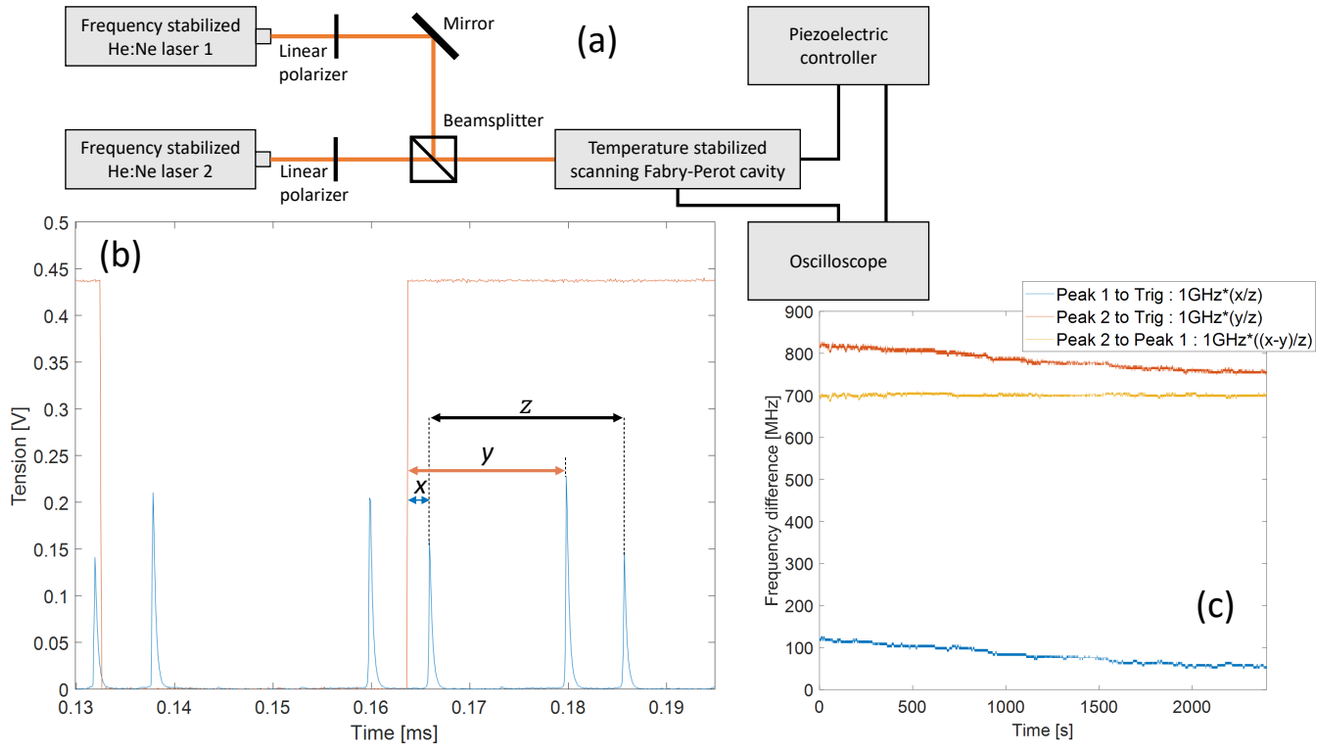

FIG. 2. (a) Experimental setup for the characterization of the frequency stability of the He:Ne reference laser. Two stabilized He:Ne lasers are injected in a temperature-stabilized Fabry-Perot cavity (FSR = 1 GHz). The cavity length is swept over more than an FSR by means of a piezoelectric actuator. (b) Zoom on a small portion of the data recorded with the oscilloscope. The relative positions x and y are measured with respect to the trigger signal associated to a specific position of the piezo ceramic sweep. (c) Plots of $x/z*1$GHz in blue, $y/z*1$GHz in red and $(x-y)/z*1$GHz in yellow. RMS fluctuations of 3 MHz are observed on the yellow curve on the 2500 seconds measurement time.

Supercontinuum light source

The broadband source currently employed is a Fianium SC450-4 supercontinuum (SC), emitting a total power of 4W distributed over the 400-2000 nm spectral range. It is a pulsed source working at 40 MHz. The beam diameter is equal to 4.4 mm at 633 nm ($1/e^2$ criterion). It is equipped with a filter splitter with two outputs covering respectively the 400-950 nm and the 950-2000 nm spectral ranges. Optical edge filters placed at the output of the SC allow to further restrict the spectral range. This restriction is necessary to match the cut-off wavelength of dichroic mirrors and the reflectivity curves of the high-reflectivity cavity mirrors but also to avoid aliasing[25]. The use of the SC as a light source in the FTS presents several advantages compared to conventional light sources commonly employed in such instruments. Indeed, light issuing from the SC is already collimated, facilitating its injection in the FTS (no Jacquinot stop and no collimating optics are required), but also in the enhancement optical cavity. It also presents a high brightness over a large spectral range, conserving the multiplex advantage while increasing the signal strength. However it presents larger fluctuations in intensity, compared to conventional light sources, requiring some noise compensation schemes. A typical technique consists in using differential detection methods (see the section concerning auto-balanced detection scheme)[26,27].

Even though the MIRA 900 femtosecond laser was already successfully injected into the FTS, most of the results presented in this article were obtained with the SC.

Translation stage

The OPD necessary to generate the interferograms is induced by a carriage moving along a 1.5 m translation stage. The carriage moves thanks to a screw shaft coupled to a DC motor and it is guided by a dovetail slide. A coding unit allows to measure the carriage velocity and a feedback loop ensures that the carriage velocity remains near its setpoint. Two stop sensors are symmetrically placed on both sides of the optical contact position. The distance separating the optical contact position from the stop sensors determines the resolution of the measurement. A Labview routine forces the carriage to travel back-and-forth between the two sensors. For each travel, acquisition at constant time intervals is triggered 1 second after the carriage starts moving. When designing the carriage, it is relevant to include alignment degrees of freedom on one of the two retroreflectors since it allows dissociating the proper alignment of mirrors M2, M3, M4 and M5 from the maximization of the overlap of the two beams at the output of the interferometer. In our case, two translation stages with mi-

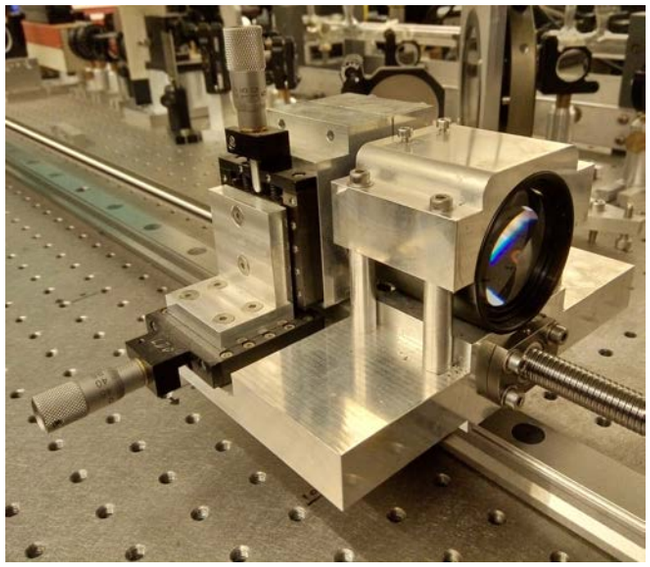

FIG. 3. Carriage with the two retroreflectors placed back-to-back. One of the retroreflectors is mounted on two translation stages with micrometers screws to maximize the overlap of the two beams at the outputs of the interferometer.

crometer screws were employed, as shown in Figure 3.

We currently limit the carriage velocity to 0.6 cm/s because of some mechanical concerns. At higher velocities, the screw shaft starts vibrating with a relatively high amplitude. There are several flaws on the current mechanical design : the screw diameter (1 cm) is too small for its length (150 cm) leading to bending of the shaft under its own weight, ultimately resulting in a poor mechanical loading of the drive nut placed on the carriage. Also, the screw shaft thread of 2 mm is too small for a continuous scan interferometer because it imposes a significant rotating speed before the carriage reaches a decent linear speed. Finally, the DC motor is directly coupled to the screw shaft so that the motor does not work at its nominal speed and the small fluctuations in its angular speed are directly transmitted to the shaft. However, even with these shortcomings, we show in section IV B that it has limited impact on the resampling process of the interferogram and in section V A that there are minor consequences on the instrumental lineshape function (ILS). Obviously, upgrading the translation stage will improve the signal-to-noise ratio of each scan but it will also considerably decrease the time needed to acquire them since higher carriage velocities will be possible.

Finally, when adjusting the carriage velocity, one has to be careful regarding the bandwidth of the detectors employed in the instrument. Indeed the temporal frequency content of the broadband light source interferogram and that of the He:Ne interference pattern depend on the carriage speed, imposing an upper limit independent of that imposed by faulty mechanics.

Auto-balanced detection scheme

Since retroreflectors are used instead of mirrors, it is possible to measure both outputs of the interferometer simultaneously and hence to measure the interferograms in an auto-balanced scheme. Auto-balanced detection allows to double the measured signal since the interference patterns of the two outputs are out of phase by 180 degrees, while removing fluctuations in intensity of the broadband source which are common to the two outputs. These fluctuations in intensity can be induced either by frequency-to-amplitude noise when coupling a frequency comb to an optical cavity[3,16] or by the use of the supercontinuum as the broadband light source.

Influence of the auto-balanced detection scheme on the SNR was investigated for the SC coupled to the FTS. To do so, the SC bandwidth was limited using a 10-nm wide bandpass optical filter centered at 1.4 μm and the spectrum was recorded with the FTS by co-adding four interferograms for the cases when a single output is measured and when both outputs are measured. The power of the SC was adjusted to have the same centerburst amplitude for the two situations to be comparable. For each case, a water transition at 7092.5 cm^{-1} was fitted and was compared to the noise level. We observed that the SNR with the auto-balanced detector was improved by a factor 2.6.

The auto-balanced detector was inspired from the circuitry presented in Ref.[28] and fabricated in-house. The detector photocurrents are subtracted, and the difference of the DC currents is kept to zero by means of a feedback loop, leading to an adjustement of the gain. The signal common to both channels is suppressed when taking the difference between the two channels while the interferometric signals which are out of phase by 180 degrees are reinforced[3].

Two dichroic mirrors are placed at each output arm of the interferometer. The dichroic mirror DM2 permits to separate the SC and the He:Ne beams in order to detect the He:Ne beam alone on a Si photodiode. Since there was still some light of the He:Ne laser reaching the right-hand-side photodiode of the auto-balanced detector, a second dichroic mirror DM3 was placed and simply serves as an optical filter. The two dichroic mirrors DM4 and DM5 in the second output arm guarantee that the two photodiodes of the auto-balanced photodetector observe a similar scene. A delay line ensures that the beams in the two output arms of the instrument travel the same distance before reaching the photodiodes. By doing so, we reassure us in the fact it will not be a concern. However, the influence of the delay line on the behaviour of the auto-balanced detection scheme was not investigated.

Optimization of the alignment and of the relative intensities on the two photodiodes is obtained by chopping the SC light source and by displaying the output of the detector on an oscilloscope. The amplitude of the observed square-like pattern is first maximised for each photodiode while the second one is covered. The relative beam intensities reaching the two photodiodes are then adjusted using a variable neutral density filter placed in one of the two arms. The subtraction of the two signals gives then a flat line on the oscilloscope at the exception of transient spikes at the times of rising and falling edges

of the square-like patterns.

Optical cavity

The gaseous sample is placed in a glass cell on which high-reflectivity mirrors (HRM) can be mounted. The two HRM are placed in optical mounts with o-rings to seal the cell. Annular piezo-actuators permit to displace the two mirrors over a distance of a few microns. Tightness of the cell is guaranteed by fixing the actuator to the other parts of the mount with low vapor pressure epoxy (Torr Seal). Figure 4 shows a picture of the optical mounts. This design presents the advantage of simplicity but it suffers from a poor bandwith when used in a feedback loop. Indeed, the first mechanical resonance of these mounts at 130 Hz limits the frequency of the feedback loop when locking the cavity to either the frequency comb or another frequency-stabilized laser[29]. Currently, no length stabilization of the cell is implemented. Instead, a triangle waveform at 100 Hz is applied on the mount to blur away the eventual frequency drift of the optical cavity due to fluctuations in its length. The two plano-concave HRM have a radius of curvature of 1 m and a reflectivity higher than 99.85% on the range of wavelengths extending from 630 nm to 1140 nm (Chirped mirrors 103521 from the Layertec catalog). They are placed 88 cm apart, on both sides of the cell tube containing the gas sample. In order to mechanically decouple the two mirrors from the cell and to allow for the alignment of the optical cell, the mirror mounts are connected to the cell via bellows. The mirror mounts are placed in Thorlabs Polaris holders which present the advantage of clamping the mirror mounts in the axial direction, leading to a better damping of the vibrations. Proper mode matching was not achieved, but coupling of the SC with the cavity was improved by focusing the beam at the centre of the cavity with a lens of focal length 750 mm. A second lens with the same focal length was placed at the output of the cavity, 750 mm away from the centre of the cavity. Two apertures on both sides of the cavity allow to overlap the supercontinuum laser with a He:Ne laser. Alignment is performed with the He:Ne laser and a CCD camera at the output of the cavity to observe the spatial distribution of the output modes in order to optimize the alignment on the TEM_{00} mode. The cavity is supposed to be aligned for the supercontinuum as well since the He:Ne and supercontinuum beams are overlapped. The display of the TEM_{00} on a screen is useful when placing the sample cell under vacuum. Indeed, the pumping down of the cell leads to a misalignment of the cell which can be compensated by performing a differential pumping with a needle valve while maintaining the displayed mode unchanged by continuously re-adjusting the mirrors alignment.

IV. DATA PROCESSING

A peculiar feature of FTS is that the observations are made in a conjugate space and that the measurements can only be interpreted after applying a mathematical operation : the Fourier transform. It means that the measured data need to be properly processed in order to retrieve the recognisable information, *i.e.* the irradiance spectrum. The data processing implies a series of operations that have to be applied in a precise order. This is the topic of section IV A. The conjugate variables in the Fourier transform of a FTS are the OPD and the wavenumbers. The sampling is performed at constant time intervals and since there are fluctuations in the carriage velocity, the interferogram needs to be resampled on a constant OPD grid. When processed at the software level, this is usually the bottleneck of the data processing pipeline because of the huge number of interpolations that have to be performed. We found an astute way to overcome this difficulty, allowing on-the-fly interferogram resampling. Section IV B details the resampling algorithm.

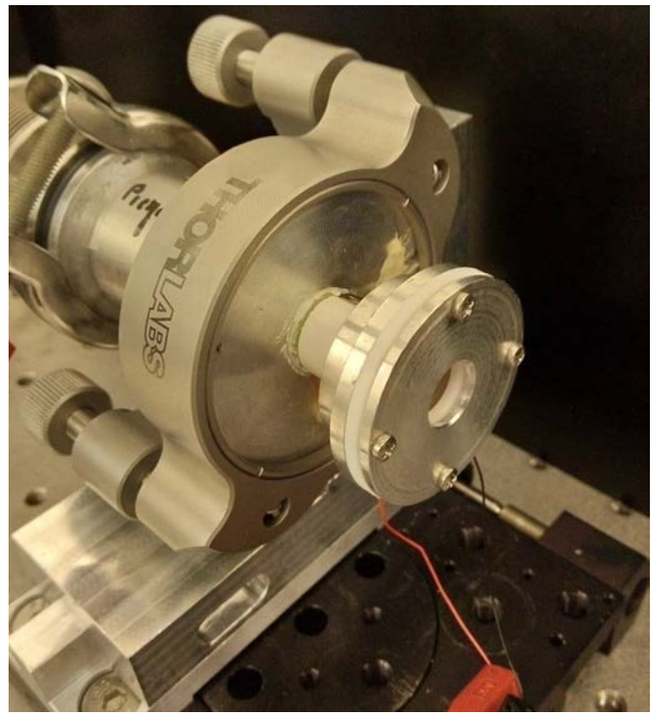

FIG. 4. Piezo-actuated vacuum-tight optical mounts for the high-reflectivity mirrors of the optical cavity.

A. Data processing pipeline

The data processing pipeline of the FTS is presented in Figure 5. The order in which the different steps are performed relies on Refs.[30–32]. Data from both the He:Ne and the SC channels are simultaneously sampled at constant time intervals with a 24 bit Analog-to-digital converter (PXI-5922 ADC from National Instruments) and saved in two different binary files. Both data acquisition and carriage displacement are controlled within the same Labview program. About 4 points per period of the He:Ne interference pattern are recorded. The sampling frequency is therefore imposed by the carriage velocity. For example, when the carriage moves at 0.6 cm/s, the

sampling frequency is equal to 150 kHz. The data processing pipeline was implemented in such a way that it does not depend on the sampling frequency, allowing for a great flexibility in the choice of the carriage velocity.

The first step of the data-processing pipeline consists in filtering the two channels with finite-impulse response (FIR) bandpass filters in order to remove both high-frequency and low-frequency components. A prior knowledge of the spectral range of the light sources allows to estimate the two cut-off frequencies. Moreover, if about 4 points per period of the He:Ne laser are effectively measured, the passband of the two signals does not change when they are expressed in terms of normalized frequency (*i.e.* frequency divided by the Nyquist frequency), meaning that the coefficients of the FIR filters do not have to be modified when changing the carriage velocity. Chapter 8 of Ref.[33] gives further information concerning the design of FIR filters.

In order to retrieve the spectrum from the interferogram, a fast Fourier transform (FFT) is applied. It requires the knowledge of the interferogram on a constant OPD grid since the conjugate variables in the Fourier transform are the OPD and the wavenumbers (cf. section II). This constant OPD grid can be obtained by determining the exact times of the zero-crossings of the sine-like interference pattern of the He:Ne reference laser. The interferogram is then interpolated at these specific times. Description of the algorithms for zero-crossing determination and interferogram resampling are given in section IV B.

The centerburst of the double-sided resampled interferogram is placed at the centre of the vector containing the samples. Interferograms are truncated on both extremities to ensure that all the datasets contain the same number of samples, permitting interferogram co-addition. In practice, we take the highest power of 2 for better performances of the FFT algorithm. The truncation on both extremities also ensures that no data is taken during starting/ending phases of the carriage translation. Since interferograms are measured for back-and-forth displacements of the carriage, one vector out of two is flipped right-to-left to ensure that every entry of the different vectors containing the interferograms always corresponds to the same OPD value.

Once all the interferograms are co-added, the resulting interferogram is apodized in order to reduce the ringing due to the instrumental lineshape function. The apodizing function employed is the one described by Naylor *et al.*[34]. The last step before applying the Fourier transform consists in removing the parasitic centerbursts due to multiple reflections in the optics (no wedged optics is employed), as depicted in Figure 6(a). If they are not removed, a fringing effect is present in the resulting spectrum, blurring away spectral lines (see Figure 6(c)). Setting these parasitic centerbursts to zero somehow corresponds to applying a notch filter in the constant OPD domain, leading to the suppression of the fringing effect on the spectrum while revealing spectroscopic information, as shown in Figure 6(f). Further details are given in Ref.[32]. As expected, the more the light source is coherent, the more the fringing effect is important. Indeed, much stronger parasitic centerbursts are observed when using the femtosecond laser, compared to the supercontinuum light source.

The last step of the data processing pipeline consists in applying the phase correction to the spectrum. The phase error is mainly caused by three factors : (1) there is little chance that the actual ZPD point is actually sampled, (2) there is some unbalanced dispersion in one arm of the interferometer, leading to non-symmetrical interferograms and finally (3) electronics employed for digitalizing the interferogram is frequency-dependent, ultimately resulting in frequency-dependent time delays[35]. This last point is also one of the main motivations to have a translation stage with a velocity as constant as possible. Information concerning the phase is obtained from the Fourier transform of a double-sided interferogram. However, most of the commercial FTS record single-sided interferograms. They usually measure a small portion of negative OPD and extrapolate the phase on the high-resolution interferogram in order to correct it. Commonly used phase-correction algorithms are described in Refs.[36,37]. The measurement of single-sided interferograms presents the advantage of reducing by almost a factor two the translation stage length and the amount of data recorded for a single dataset, but this is done at the expense of an assumption on the phase. In our instrument, the interferograms that are recorded are double-sided, allowing a straightforward correction of the phase without any assumption on it. The extra number of data per dataset contains redundant information, increasing the SNR by $\sqrt{2}$ while doubling the measurement time[18]. From that perspective, it is thus a free operation because it reduces by a factor 2 the number of single-sided interferograms we would have coadded to obtain the same SNR.

B. Constant OPD grid generation

Both the reference and the SC signals are sampled at the same times, meaning that to a given index in the two vectors corresponds an identical sampling time. In order to evaluate the interferogram on a constant OPD grid, the precise times, or equivalently the fractional indices, of the zero-crossings of the He:Ne interference pattern must be determined. Indeed, they are half a wavelength apart. The interferogram is then resampled at these times. Choice was made to use fractional indices instead of time in order to make the data-processing pipeline independent of the sampling frequency and the carriage velocity. The only condition to fulfil is to record about 4 samples per period of the He:Ne interference pattern. The method suggested by Yang *et al.*[30] to retrieve the uniform OPD grid from the data sampled at constant time intervals consists in interpolating between the data to determine the zero-crossings fractional indices. To do so, the He:Ne signal is first zero-padded to increase the sampling grid by a factor 8. Location of the zero-crossings is then roughly estimated by finding changes in sign between adjacent samples of this denser grid. The 3 samples before and the 3 samples after the zero-crossings are approximated by a cubic function and the root of this cubic function located in the vicinity of the two middle samples is evaluated. The root is the fractional index at which the interferogram should be interpolated. This is illustrated in Figure

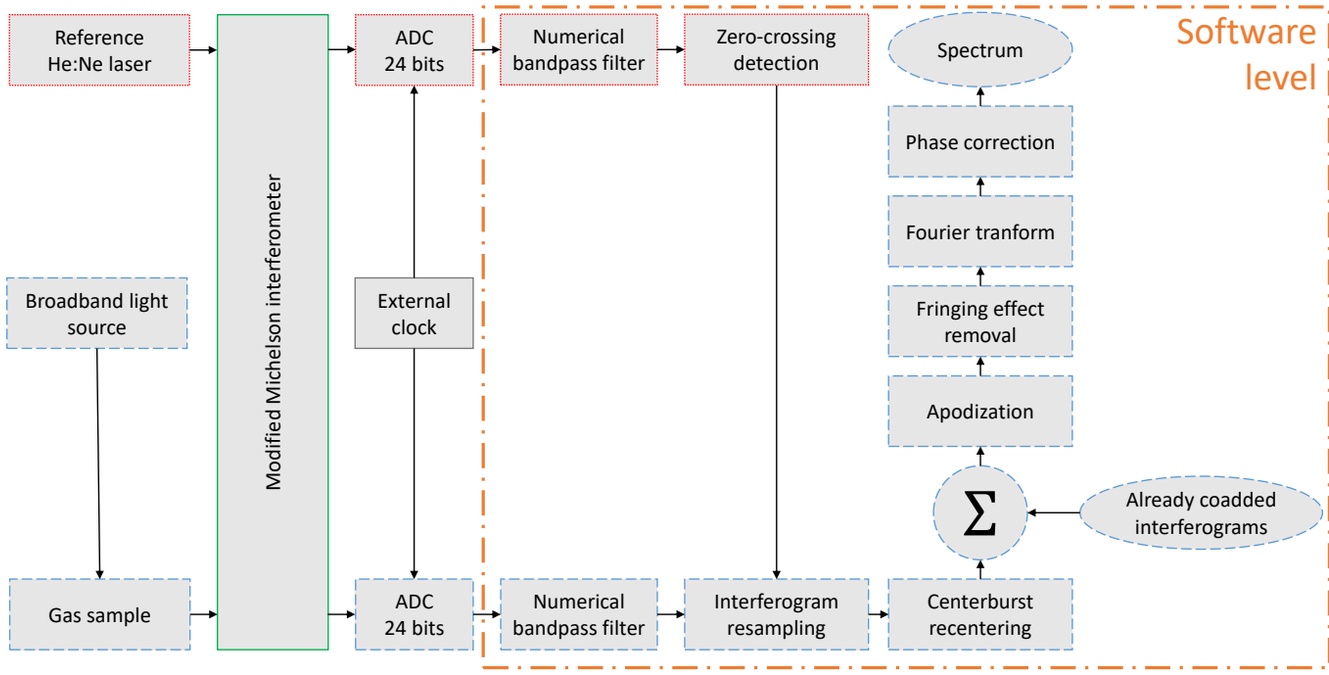

FIG. 5. Data processing pipeline of the Fourier transform spectrometer. The blue dashed frames represent the interferogram channel, the red dotted frames are for the He:Ne reference channel and the green plain frame is common to both channels. The orange frame with an alternance of dashed lines and dots indicates the part of the process that is performed at the software level. Rectangular frames are stages in the data-processing pipeline. The oval frame labelled *Already coadded interferograms* is a vector containing all the previously recorded interferograms that were already treated up to the *centerburst recentering* stage included.

7. When spectra are recorded at full resolution of the FTS, more than 17 millions of interpolations should be performed, meaning that more than 17 millions systems of equations have to be solved, which is computationally expensive. Fortunately, it is possible to take advantage of the fact that the abscissa are evenly spaced since they correspond to successive indices.

Finding the polynomial that best approximates the set of data involves solving the following system of linear equations :

$$\begin{bmatrix} (k-2)^3 & (k-2)^2 & (k-2) & 1 \\ (k-1)^3 & (k-1)^2 & (k-1) & 1 \\ k^3 & k^2 & k & 1 \\ (k+1)^3 & (k+1)^2 & (k+1) & 1 \\ (k+2)^3 & (k+2)^2 & (k+2) & 1 \\ (k+3)^3 & (k+3)^2 & (k+3) & 1 \end{bmatrix} \begin{bmatrix} p_1 \\ p_2 \\ p_3 \\ p_4 \end{bmatrix} = \begin{bmatrix} y_{k-2} \\ y_{k-1} \\ y_k \\ y_{k+1} \\ y_{k+2} \\ y_{k+3} \end{bmatrix}. \quad (5)$$

where $k-2$, $k-1$ and k are the indices of the samples y_{k-2}, y_{k-1} and y_k just before the zero-crossing, $k+1$, $k+2$ and $k+3$ are the indices of the samples y_{k+1}, y_{k+2} and y_{k+3} just after it and p_1, p_2, p_3 and p_4 are the coefficients of the third degree polynomial $y = p_1x^3 + p_2x^2 + p_3x + p_4$ that best fits the 6 samples. The first matrix in this problem is the so-called Vandermonde matrix. Finding the four coefficients of the polynomial implies to find the the pseudo-inverse of the Vandermonde matrix for each of the millions of zero-crossings that need to be found, which is time-consuming. Fortunately, in our case, this matrix has a similar form for all the polynomials that have to be evaluated, at the exception of the value of k. The problem can be shifted around zero by setting $k = 0$. A single pseudo-inverse has to be found for all the zero-crossings, reducing considerably the execution time. The value of the determined zero-crossing is then simply shifted back by k after having being determined around zero. Finding the p coefficients now simply requires evaluating 4 products. The root corresponding to the index of the zero-crossing is then found using the Newton-Raphson method. The 17 millions of zero-crossings are evaluated in less than the time needed for the carriage to travel its full travel with Matlab on a typical laptop (Intel i5-644HQ CPU working at 2.6 GHz), allowing on-the-fly data processing.

Once the fractional indices i of the zero-crossings are determined, the interferogram needs to be ressampled at these specific times. This has to be done numerically. The sinc interpolation was preferred to the simpler approach of cubic interpolation because it led to much better results. Indeed, we generated a simulated interferogram of a black body spectrum from which we had access to the analytical value of the interferogram for any OPD. We compared the relative error between the analytical value and the resampled value for both the cubic and the sinc interpolations for random values of the OPD. We found that the relative error was smaller by at least

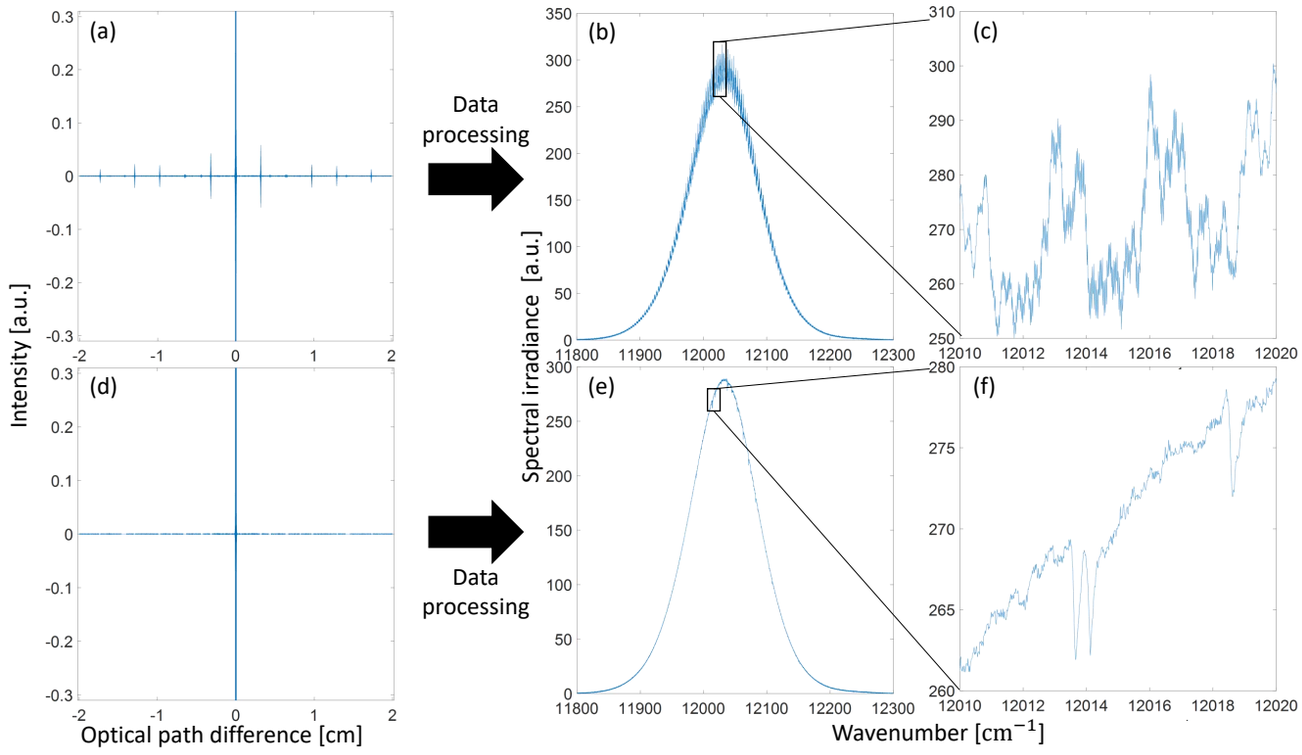

FIG. 6. Fringing effect from both the interferogram (a) and spectrum perspectives (b). Removal of the parasitic centerbursts in the OPD domain (d) strongly attenuates the modulations in the frequency domain (e). Water absorption lines that could not be distinguished in (c) are now clearly visible in (f). The spectra correspond to the FFT of 12 co-added interferograms taken with the MIRA900 femtosecond laser emitting between 815 and 845 nm and travelling approximatively 10 m in free space. Figures (a) and (d) are a zoom of the complete interferogram (about 32 cm of OPD) in the vicinity of the centerburst. The spectrum was taken at a resolution of 0.015 cm^{-1}.

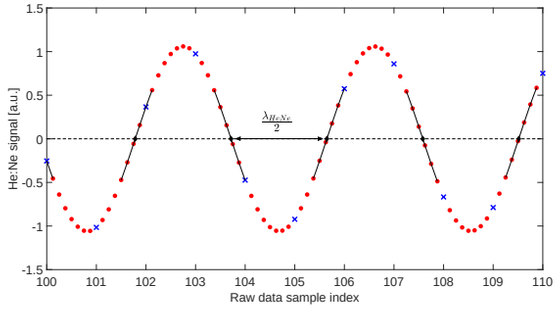

FIG. 7. Estimation of the zero-crossings of the He:Ne interference pattern. Blue cross : experimental data, red dots : interpolated data (zero-padding), black curves : cubic approximation, black diamond : estimated zero-crossings.

one order of magnitude for the sinc function. Thanks to the prior use of the two FIR filters (see Figure IV A), the problem is properly band-limited. Moreover, samples are evenly spaced in the time domain. A better approach thus consists in using sinc interpolation. It can be shown (see Ref.[33] for a good overview of the sinc interpolation) that the exact value of a signal $y(t)$ at any time t can be estimated from the knowledge of this signal sampled at uniform time intervals using the following relationship :

$$y(t) = \sum_{n=-\infty}^{+\infty} y[n] * \mathrm{sinc}\left(\frac{\omega_s(t-nT_s)}{2\pi}\right), \qquad (6)$$

where $y[n]$ is the signal sampled at time n, ω_s the sampling frequency and $T_s = \frac{2\pi}{\omega_s}$ the sampling time. For convenience, equation (6) is re-expressed in terms of the fractional index i rather than the time t.

$$y(i) = \sum_{n=-\infty}^{+\infty} y[n] * \mathrm{sinc}\,(i-n)\,. \qquad (7)$$

Theoretically, finding the exact value at the zero crossing, $y(i)$, implies to use an infinite sum. In practice, the sinc function rapidly tends to zero, allowing for the use of a finite summation. Evaluating the sinc function for each term of the sum of equation (6) and for a large number of values (up to 17 million times for interferograms at full resolution) is too time demanding. In order to tackle this challenge, the interval between two measured points is discretized m times. Brault[38] introduced the idea to store vectors equidistant in times including one of the m interpolating points and gathering $n/2$ values of the sinc function on each side of the considered point. Those vectors are rows stored in a matrix named kernel resulting in an array of $m \times n$ values (see equation (9)). Those

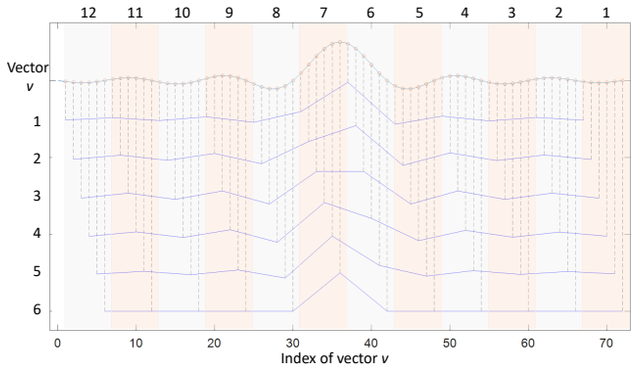

FIG. 8. Illustration of the filling process of the matrix of equation (9) for $m = 6$ and $n = 12$. The sinc function is evaluated in 72 values which are then parsed in 6 rows of length 12.

values are evaluated only once for the millions of points which need to be interpolated. Estimating the interferogram at a specific fractional index i now consists in choosing the index l (with $1 \leq l \leq m$) which is the closest to $(i-k)/m$, in this array and to perform an element-by-element product with the $n/2$ values before the zero-crossing fractional index and the $n/2$ values after it and to add together the n obtained values. The construction of this $m \times n$ matrix follows the principle illustrated in Figure 8 for $m = 6$ and $n = 12$. In this illustration, the upper curve is a sinc function evaluated at $6 \times 12 = 72$ discrete and equidistant values. These 72 values are parsed in 6 row vectors of 12 equidistant (in time) values that built up the kernel. The first row vector contains the 1st, 7th, 13th, etc. values of the upper sinc function, the second row vector contains the 2nd, 8th, 14th, etc. values, and so forth for the four remaining rows.

The choice of the appropriate filter, *i.e.* the row l of the kernel, is made by evaluating the following expression :

$$l = 1 + \text{floor}(m * (i-k)), \tag{8}$$

where k is the index of the previous sample and i the fractional index at which we want to interpolate the signal. The term $+1$ comes from the fact that the first index of an array is 1 in Matlab. The function floor is a rounding function towards the lower integer.

$$\text{kernel} = \begin{bmatrix} v(m(n-1)+1) & \dots & \dots & v(2m+1) & v(m+1) & v(1) \\ \vdots & \vdots & \vdots & \vdots & \vdots & v(2) \\ \vdots & \vdots & \vdots & \vdots & \vdots & v(3) \\ \vdots & \vdots & \vdots & \vdots & \vdots & \vdots \\ \vdots & \vdots & \vdots & \vdots & \vdots & v(m-1) \\ v(mn) & v(m(n-1)) & \dots & v(2m) & v(m) & \end{bmatrix}. \tag{9}$$

The last step of the interpolation process is the evaluation of the following sum :

$$y(i) = y(k + \frac{l}{m}) = \sum_{j=1}^{n} y\left[k - \frac{n}{2} + j\right] * \text{kernel}(l, j). \tag{10}$$

This is illustrated in Figure 9. This figure depicts on the top the 72 points sinc function and the associated 1th row of the kernel is outlined using dashed lines. In practice, in our data processing pipeline, the values $n = 64$ and $m = 1024$ were chosen. They were determined by performing convergence studies on simulated interferograms. Moreover, in order to reduce eventual artefacts due to the finite number of terms in the summation of expression (6), the sinc function is multiplied by a Gaussian function, as suggested by Yang *et al.*[30].

Because of the fluctuations in the carriage velocity, the samples evenly spaced in the time domain are not evenly spaced in the OPD domain. But the values of the sampled interferogram only have a true meaning in the OPD domain. Brault suggested to adapt the digital filter to the instantaneous velocity of the carriage in order to correct the velocity fluctuations. The method is better described in the article of Yang *et al.*[30]. We tried to implement this velocity correction and even if it generally gave better results on the resampling process, it ironically failed when velocity fluctuations were too severe. This velocity correction is therefore not used in the data analysis.

In order to verify the correct behavior of the whole interferogram resampling process and to study the consequences of the velocity fluctuations on the resampling, the He:Ne interference pattern was resampled at the times of its zero-crossings. If there was no error, the values obtained would be exactly equal to zero. Any deviation Δy from zero is therefore imputed to an error Δx on the position of the zero-crossing. To express Δx in terms of distance, a Taylor expansion of a sine wave around zero is performed as follows :

$$\Delta y = A \sin(\frac{2\pi}{\lambda}\Delta x) \approx A\frac{2\pi}{\lambda}\Delta x - \frac{A}{6}\left(\frac{2\pi}{\lambda}\Delta x\right)^3 + \dots \tag{11}$$

Where λ is the wavelength of the He:Ne reference laser and A the amplitude of the interference fringes. Keeping only the first order term and isolating Δx leads to :

$$\Delta x = \frac{\lambda \Delta y}{2\pi A}. \tag{12}$$

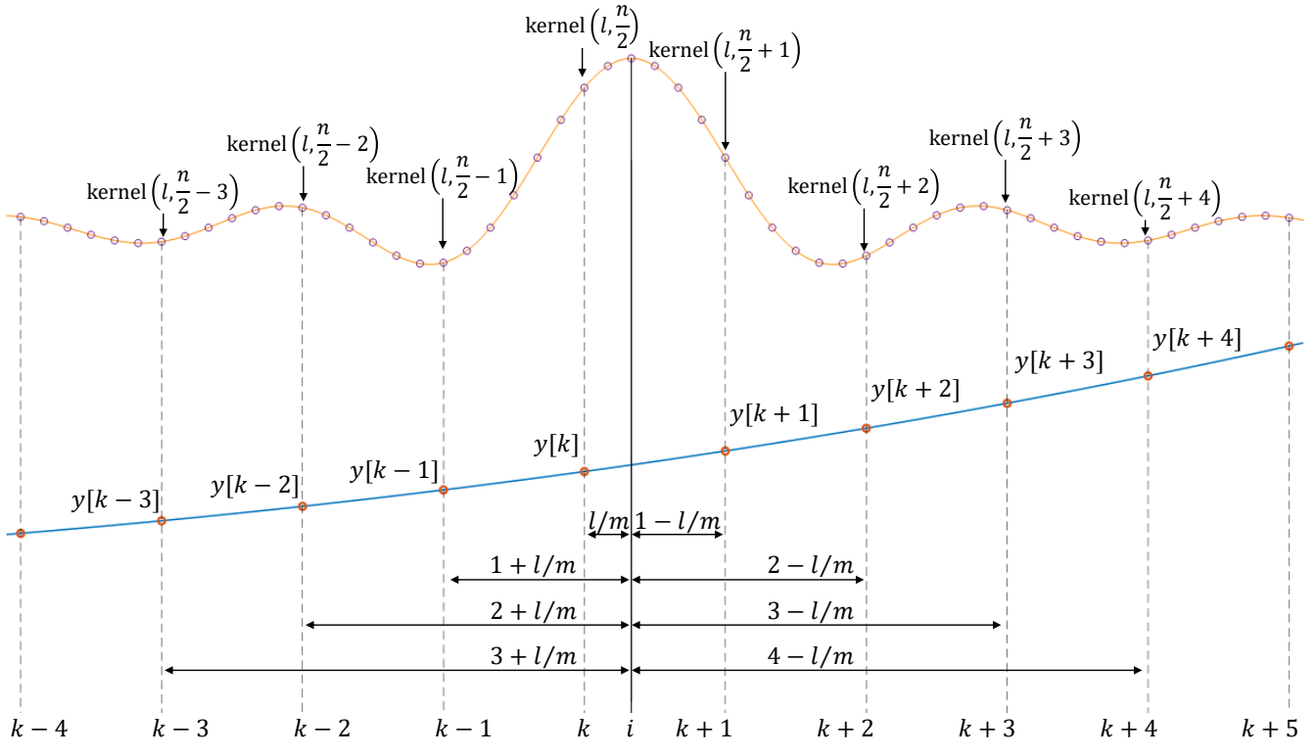

FIG. 9. Brault resampling method. The blue curve corresponds to the signal, the red dots are the sampled values of the signal and the orange curve corresponds to the sinc function used to build the resampling kernel. The purple dots are the discrete values of the resampling kernel stored in the matrix of equation (9). Distance between the k^{th} sample and the fractionnal index i at which the signal is resampled is l/m.

A small trace of the resampling error with respect to the position is shown on the bottom plot of Figure 10 while the two upper plots correspond to the velocity fluctuations and the fringe visibility with respect to the position. The instantaneous velocity was evaluated by using the knowledge of the times of the zero-crossings that are spatially equidistant of half a wavelength of the He:Ne laser. Both the fringe visibility and the instantaneous velocity seem to vary with a periodic pattern. This is confirmed by a spectral analysis by means of their Fourier transforms in section V A. We can also observe that the error on the zero-crossing location tends to increase when the velocity fluctuations are large meaning that the mechanics actually impacts the resampling process. However, no structured pattern was observed on the Fourier transform of the resampling error with respect to the position. This is fortunate since a periodic error in the interval at which the interferogram is resampled would lead to the presence of a ghost line at a wavenumber $\sigma_g = \sigma_N - \sigma_l$, where σ_N is the Nyquist wavenumber and σ_l the wavenumber of the parent line[25]. Finally, even with the large fluctuations in the carriage velocity (*i.e.* about 10%), the zero-crossings locations are known with a precision better than 0.17 nm (3σ criterion), meaning that we are able to generate an OPD grid of 5.4 m long with ticks spaced by 316.4 nm with a precision better than 0.17 nm. This precision is larger than any fluctuation in the wavelength of the reference laser due to variations in the laboratory pressure and temperature, i.e. change in the air refractive index, by at least one order of magnitude.

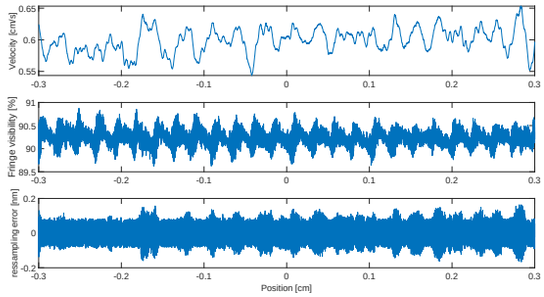

FIG. 10. Velocity fluctuations and their consequences on the fringe visibility and the resampling in the spatial domain.

V. PERFORMANCES

We first characterize the instrumental lineshape function (ILS) of the instrument in section V A. It was experimentally measured by means of an external cavity diode laser (ECDL) at 778.2 nm. Consequences of velocity fluctuations on the ILS are underlined in the same section.

The characterizations of both the wavenumber axis accuracy and the sensitivity of the setup were performed on wa-

ter desorbing from the cell walls. The wavenumbers associated to the transitions and their corresponding line intensities were retrieved from the 2008 Hitran database[39]. The spectrum is shown in Figure 11. It was measured at a resolution of 0.015 cm^{-1}. To obtain the spectrum, 1084 interferograms were co-added and the parasitic centerbursts were removed. Each interferogram takes 30 seconds to be recorded. The oscillations in the baseline are imputed to fluctuations in the reflectivity of the HRMs of the 88 cm long cavity. The strong cutoff at 14300 cm^{-1} is due to the use of an edgepass filter while the gentle cutoff at 10500 cm^{-1} is caused by the filter splitter of the Fianium supercontinuum. The small spectral irradiance in the range of wavenumbers between 12600 cm^{-1} and 13600 cm^{-1} is due to the the cavity mirrors reflectivity of nearly 100% in this region of the spectrum. The cell was pumped down with a rough-vacuum pump. The pressure in the cell was measured with a Pirani gauge and varied from 2 Torr to 4 Torr during the whole measurement time.

The wavenumber-axis accuracy, presented in section V B requires the knowledge of the absorbance spectrum while the determination of the sensitivity of the instrument, detailed in section V C, necessitates to know the transmittance spectrum. The experimental measurement of these two physical quantities implies the measurement of a background spectrum, *i.e.* a spectrum in the absence of the sample. Since we measured the residual traces of water in the cavity, the background spectrum was unaccessible. To overcome this difficulty, a simulated transmittance spectrum from the Hitran database was utilized to generate a mask employed in a weighted penalized least squares fit of the spectrum. This fit is also known as the weighted Whittaker smoother algorithm[40]. Since the peaks are hidden by the mask, the result of the fit is considered to be the background spectrum. The transmittance is then evaluated by dividing the spectrum by the estimated background. The absorbance is finally obtained by taking the opposite of the decimal logarithm of the transmittance.

Finally, we benchmarked our instrument with another recent setup performing FT-IBBCEAS with a FTS and a supercontinuum. This comparison is given in section V D.

A. Instrumental lineshape function

Ideally, the Fourier-transform of the interferogram recorded with the instrument should give access to the true spectrum. In practice, this is not the case because of the inherent practical and physical limitations of the instrument such as the finite length of the translation stage, the natural divergence of the light beams, the frequency-dependent response of the electronics, the imperfect mechanics, etc. All these non-idealities will modify the spectrum by convolving it with a function : the ILS that can be interpreted as the instrumental response to a monochromatic source[4].

In order to characterize the ILS of the instrument, a temperature-stabilized external cavity diode laser (ECDL) working at 778.2 nm (DL100 ECDL from Toptica) was injected in the FTS and its spectrum was measured. It is plotted in Figure 12. A single interferogram was recorded at the resolution of 0.00322 cm^{-1}. No apodization was applied prior to evaluating the Fourier transform. The spectrum looks like a typical mode emitted from a laser but we can see a structured pattern of ghost lines symmetrically located on both sides of the ECLD emission line. However, the stronger ghost lines are about 3 orders of magnitude smaller than the emission line. They are caused by some modulation of the interferogram and they are offset from the parent line by the modulation frequency[41]. In our setup, these ghost lines are imputed to the mechanics, and more specifically to periodic misalignments due to the vibrations of the carriage, ultimately resulting in a modulation of the interferogram, leading to their apparition in the instrumental lineshape function[25]. In order to justify this statement, the right wing of the ECDL emission line was shifted around zero and it was compared to the Fourier transforms of the carriage velocity and the fringe visibility of the He:Ne interference pattern with respect to the position presented in Figure 10 of section IV B. The three spectra are shown in Figure 13. We can see that most of the peaks present in the fringe visibility and velocity spectra are also present in the wings of the instrumental function, indicating an impact of the vibrations on the measured spectra. Some peaks in the ILS are not present in neither the visibility spectrum nor the velocity spectrum. They correspond to higher harmonics of the fundamental modes present in both spectra. The structured patterns present in the velocity and fringe visibility spectra can be interpreted as "events" occurring a certain number of times per turn of the screw shaft. Such an analysis can help with the identification of the causes of these vibrations. Fortunately, the presence of these ghost lines in the ILS is auspicously mitigated in the case of absorption spectra by about two orders of magnitude when compared to emission lines because of the smaller signal-to-noise ratio[41].

B. Wavenumber axis accuracy

Theoretically, a spectrum taken with a FTS is absolutely calibrated provided the wavelength of the reference laser is known. This is the so-called Connes' advantage of FTS over the other types of spectrometers. However, true FTS deviate from this ideal behaviour mainly for two reasons : (1) light of both the reference and the broadband light source are not perfectly collimated and (2) the He:Ne and the supercontinuum laser beams are not perfectly aligned[42,43]. Therefore, as for dispersive spectrometers, it is necessary to apply the internal standard method which consists in recording a spectrum with both the unknown features and features whose positions have been independently measured. The wavenumber-axis is then calibrated by correcting it so that the central wavenumbers of the known transitions match with the wavenumber-axis[44]. The wavenumber-axis is corrected by considering known spectral features spanned on a large region of the spectrum and by imposing their position using a linear regression.

In our case, the spectrum was calibrated using H_2O desorbing from the cell walls. About half of the isolated peaks above a 0.05 absorbance threshold and resulting from a single transition were automatically fitted using Gaussian functions

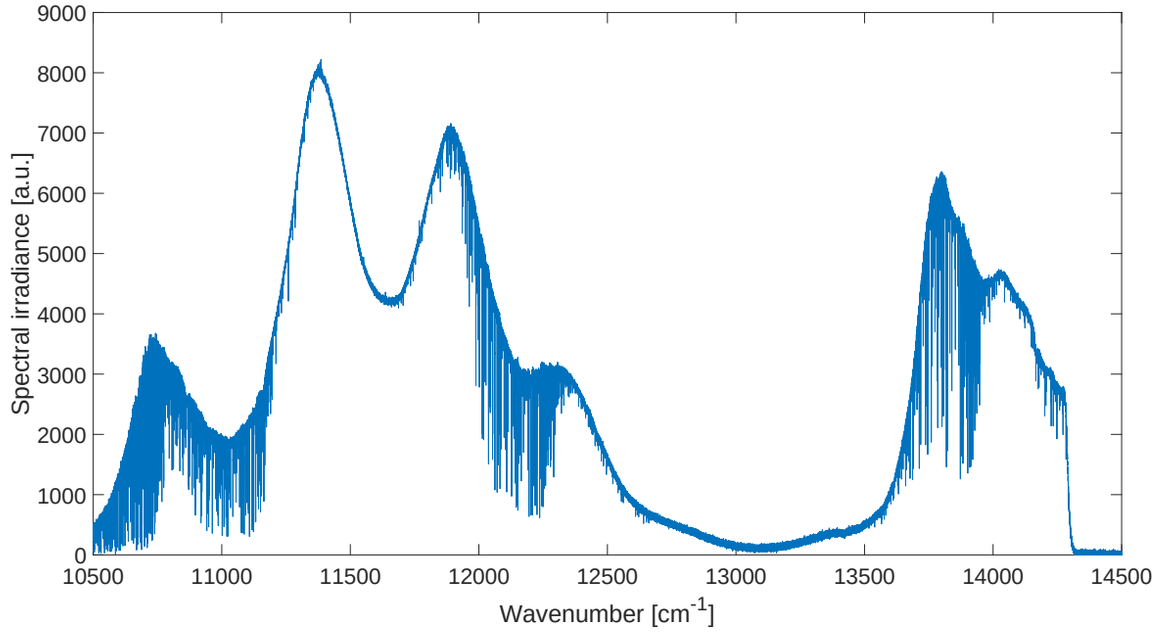

FIG. 11. Cavity-enhanced spectrum of H_2O desorbing from a 88 cm long cell at a resolution of 0.015 cm^{-1}. The pressure varied between 2 and 4 Torr during the measurement. 1084 co-added interferograms.

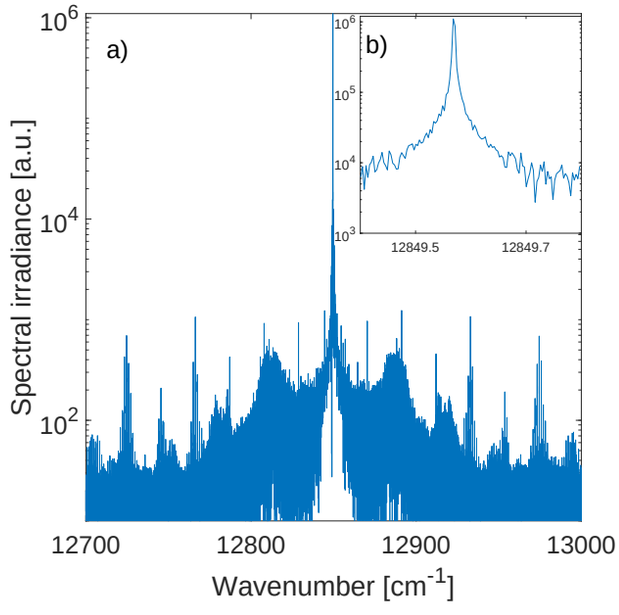

FIG. 12. (a) Instrumental lineshape function of the FTS at 12849.56 cm^{-1} (778.24 nm).(b) Zoom on the laser emission line. A single interferogram was recorded at a resolution of 0.00322 cm^{-1}.

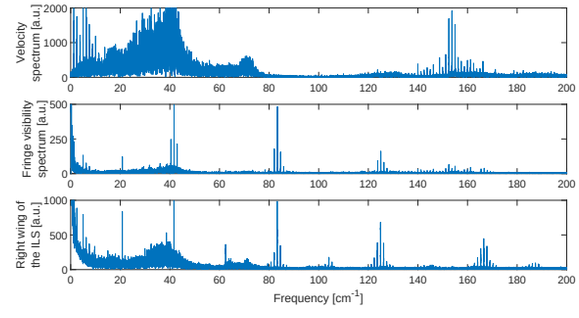

FIG. 13. Impact of the velocity fluctuations on the contrast of the He:Ne laser interference pattern and on the ILS. Top : velocity spectrum. Middle : fringe visibility spectrum. Down : right wing of the ECDL emission line shifed around zero.

in order to determine their experimental central wavenumber. Gaussian profiles were chosen on the hypothesis that pressure broadening can be neglected at 4 Torr, resulting in purely Doppler-broadened transitions. The wavenumber-axis was then corrected to impose that the experimental wavenumber of these lines matches the 2008 Hitran database[39]. The calibration process was validated by evaluating the deviation of the central wavenumber on the other half of the H_2O transitions from the ones of the Hitran database. For the sake of completeness, the deviation before calibration and for a single-line calibration are also plotted. As we can see, single-line calibration is only valid in the vicinity of the line. In the case of multiple-lines calibration, the root mean square deviation from the Hitran database was equal to 0.0017 cm^{-1} for a spectrum with a resolution of 0.015 cm^{-1} and a mean transition width of 0.046 cm^{-1} at half maximum. This value is in good accordance with Ref.[44].

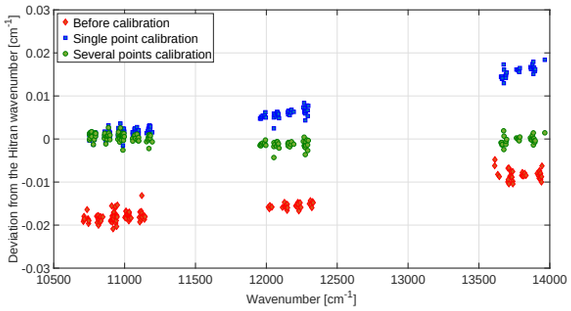

FIG. 14. Deviation of the central wavenumber of the experimental H_2O lines from the Hitran database for the spectrum presented in Figure 11 recorded at a resolution of 0.015 cm^{-1}.

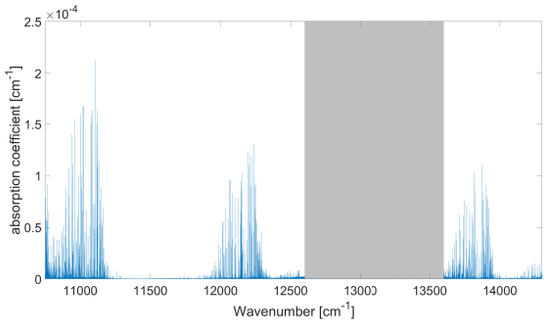

FIG. 15. Absorbance with respect to the wavenumber, evaluated using equation (14) and with the mirror reflectivity found with equation (15). The grey zone was suppressed due to a lack of signal.

C. Instrument sensitivity

Absorption spectroscopy relies on the measurement of the frequency-dependent attenuation of light after its interaction with the sample. Usually, the absorption is described using the Beer-Lambert's law which stipulates that the attenuation is proportional to the optical path through the sample :

$$\mathrm{d}I = -I(\tilde{\nu})\alpha(\tilde{\nu})\mathrm{d}l, \tag{13}$$

where $I(\tilde{\nu})$ is the intensity of light at wavenumber $\tilde{\nu}$, $\alpha(\tilde{\nu})$ is the wavenumber-dependent absorption coefficient which depends on both the line intensity and the amount of the species under study. Finally, $\mathrm{d}I$ is the intensity reduction after interacting with the sample on a distance $\mathrm{d}l$. The sensitivity of the instrument is characterized by the smallest value of $\alpha(\tilde{\nu})$ the instrument can measure, denoted $\alpha_{\min}$. As mentioned in the introduction, the sensitivity can be improved by performing CEAS measurements. When working with optical cavities illuminated by a broadband light source, the retrieval of the absorption coefficient $\alpha(\tilde{\nu})$ from the transmittance spectrum is not as straightforward as in experimental setups with multi-pass cells since the transmission spectrum of the optical cavity must also be taken into account, leading to the following complicated expression[45] :

$$\alpha = \frac{1}{d}\left|\ln\left(\frac{1}{2R^2}\left(\sqrt{4R^2+\left(\frac{I_0}{I}(R^2-1)\right)^2}+\frac{I_0}{I}(R^2-1)\right)\right)\right|, \tag{14}$$

where R is the reflectivity of the HRM, d is the cavity length, I_0 the intensity at the output of the empty cavity and I the intensity at the output of the cavity in presence of the absorbing species. In order to determine the sensitivity of the instrument, it is therefore necessary to determine experimentally the reflectivity of the HRM. This is done by measuring the absorption of a known amount of H_2O in the cavity, whose line intensities i_H are known from the Hitran database and by employing the following formula :

$$R = 1 - \frac{N d i_H}{\int\left(\frac{I_0(\tilde{\nu})}{I(\tilde{\nu})}-1\right)\mathrm{d}\tilde{\nu}}, \tag{15}$$

where N is the density (molecule $\times \mathrm{cm}^{-3}$) of water in the cavity. This equation is the one used by O'Leary *et al.*[12] and it is derived from equation (14) by imposing a high mirror reflectivity ($R \to 1$) and small losses due to absorption ($\frac{I}{I_0} \to 1$). The cavity length was equal to 88 cm, the density was obtained by supposing that the residual pressure in the gas cell was equal to 4 Torr (worst case scenario) and was only due to water desorbing from the cell walls. The denominator in equation (15) is evaluated by fitting peaks corresponding to molecular transitions of water in the $\left(\frac{I_0(\tilde{\nu})}{I(\tilde{\nu})}-1\right)$ spectrum with a Gaussian function and by using the resulting fitting coefficients in the analytical expression of the integral of the Gaussian function. To avoid poor fitting and to guarantee the validity of the formula, only peaks with transmission between 0.9 and 0.95 are considered for the determination of the mirrors reflectivity. A mean effective reflectivity $\overline{R}$ of 99.76% was estimated. Injecting this value in equation (14) allows to compute the absorption coefficient with respect to the wavenumber and therefore to estimate the sensitivity of the instrument, that is the lowest value of $\alpha(\tilde{\nu})$ that can be distinguished from the noise. A plot of the absorption coefficient with respect to the wavenumber is shown in Figure 15. A zoom of the absorption coefficient between 11920 cm^{-1} and 11930 cm^{-1} is given in Figure 16. The black dashed lines in this plot correspond to a $1\sigma = 6.5 \times 10^{-8}$ cm^{-1} noise in the value of the absorption coefficient. The red curve corresponds to the absorption coefficient of pure H_2O at 4 Torr and 293K simulated with the Hitran database. The 1σ deviation was estimated on the samples presented in Figure 16 (range of wavenumbers from 11920 to 11930 cm^{-1}) from which the molecular transitions were removed thanks to the mask discussed in the introductory part of section V.

D. Comparison with another FT-IBBCEAS setup

In order to further characterize the performances of our setup, it is benchmarked against the setup of M. O'Leary *et al.*[12] where FT-IBBCEAS was performed with a Fianium SC450-6 supercontinuum laser source and a Vertex 80 FTS from Bruker. To our knowledge, their instrument is the setup

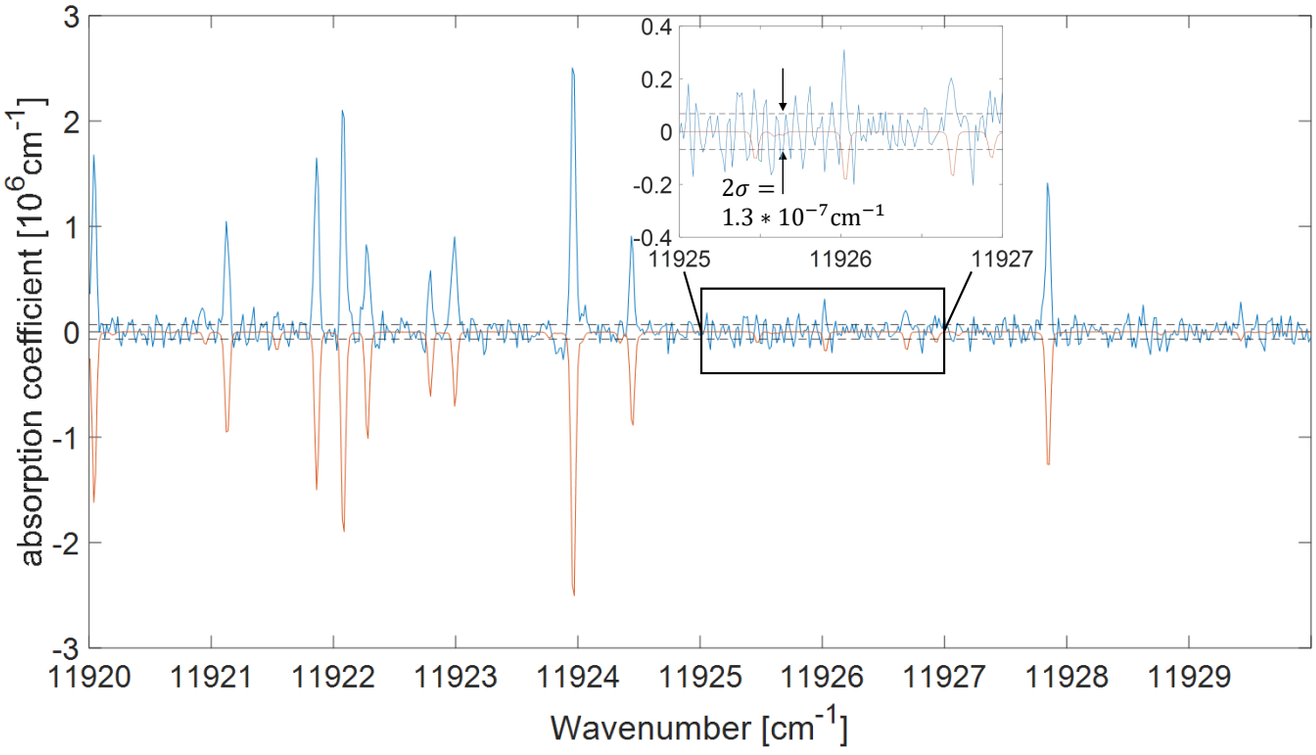

FIG. 16. Zoom between 11920 cm^{-1} and 11930 cm^{-1} of the absorbance with respect to the wavenumber presented in Figure 15. A frame with a zoom between 11925 cm^{-1} and 11927 cm^{-1} is shown. Blue : experimental absorbance. Red : theoretical absorbance ($T = 293$K, $P = 4$Torr). Black dashed lines : $\pm 1\sigma = 6.5 \times 10^{-8}$ cm^{-1} noise.

that is closest to ours. Table I compares the specifications of the two setups, along with the relevant experimental parameters.

First, we can see that the light source they used in their instrument delivers 50% more optical power than ours, allowing for the use of mirrors with higher reflectivity and for more signal. The most relevant quantity is the sensitivity coefficient since it is an indirect measurement of the SNR. Their minimal absorption coefficient is 6.5 times lower than ours. However, this value has to be manipulated cautiously. Indeed, from equation (14), we can see that optical cavities with mirrors of higher reflectivity ultimately lead to a higher sensitivity. Furthermore, they utilized an optical cavity with a length of 644 cm, against 88 cm for our optical cavity. From equation (14), we can see that our minimal absorption coefficient would be improved by a factor 7.3 at equal cavity length. Furthermore, even if we remove the shaded area of Figure 15 due to poor signal, we still cover 2800 cm^{-1} of spectral range in the near infrared, against 2000 cm^{-1} for their measurement, and this at a resolution about 10 times better. The better resolution is counterbalanced by a much longer measurement time. The dead times due to the changes in direction of the carriage were set aside from the measurement duration specified in Table I. In order to better compare the two setups, it is necessary to use a metric that incorporates all these features in a single scalar value. The absorption sensitivity per spectral element normalized to a 1-s acquisition time, denoted $\alpha'_{\min}$, found in Ref.[46], is given by :

$$\alpha'_{\min} = \alpha_{\min} \frac{\sqrt{T}}{\sqrt{M}} \left[\mathrm{cm}^{-1}\mathrm{Hz}^{-1/2} \right], \tag{16}$$

where T is the measurement time and M the number of spectral elements. This value was then multiplied by the respective cavity lengths of the two setups in order to have a single metric value that takes most of the experimental parameters into account. The values of this comparison metric and of $\alpha'_{\min}$ are also given in Table I. We can see that the two instruments have similar performances, assuring the proper working of our FTS when compared to the commercial instruments that lead the market.

VI. CONCLUSION

This article presents our experience in the fabrication of a high resolution Fourier transform spectrometer employing a supercontinuum light source coupled to a high finesse optical cavity for molecular spectroscopy in the gaseous phase. Both the hardware and software aspects were discussed. Concerning the hardware, experimental considerations and methodology were fully detailed to permit other groups to build in a modest amount of time their own high-resolution FTS. Special attention was given on the characterization of the in-house frequency-stabilized He:Ne reference laser and of the

TABLE I. Comparison of the performances of our instrument with the experimental setup of M. O'Leary *et al.*[12].

	M. O'Leary *et al.*[12]	This work
Light source	Fianium SC450-6 [6W]	Fianium SC450-4 [4W]
Spectrometer	Bruker, Vertex 80	in-house built FTS
Detector	single	autobalanced
Effective reflectivity of the HRMs [%]	99.88	99.76
Pressure [mbar]	4	5.33 (unfavorable)
Resolution $\left[\mathrm{cm}^{-1}\right]$	0.12	0.015
Spectral range $\left[\mathrm{cm}^{-1}\right]$	6000-8000	10500-14300
Effective bandwidth $\left[\mathrm{cm}^{-1}\right]$	2000	2800
Cavity length d [cm]	644	88
Minimal absorption coefficient $\left[10^{-8}\mathrm{cm}^{-1}\right]$ (1σ noise)	1.0	6.5
Measurement time [min]	60	500
Minimal absorption coefficient per spectral element normalized to 1-s acquisition time α'_{min} $\left[10^{-8}\mathrm{cm}^{-1}\mathrm{Hz}^{-1/2}\right]$	0.465	2.241
$\alpha'_{\mathrm{min}} * d$, $\left[10^{-6}\mathrm{Hz}^{-1/2}\right]$	2.99	1.97

mechanics of the carriage that induces the OPD. An original approach to the resampling of the interferogram on a constant OPD grid from its knowledge on an uniform time grid at the software level is given. Optimization of the data processing pipeline allows for on-the-fly analysis of data with any recent computer.

The performances of the instrument in terms of instrumental lineshape function, wavenumber accuracy and sensitivity were evaluated. The instrument was also benchmarked against a similar setup developed by O'Leary *et al.* (Ref.[12]). We demonstrated the feasibility of fabricating in-house a high performance Fourier transform spectrometer with limited resources.

ACKNOWLEDGEMENT

We are thankful to the *Service de Chimie Quantique et Photophysique* of the Université libre de Bruxelles (ULB) for lending us the VIS/QIT501/2 beamsplitter from Bruker. This work was supported by the Fonds de la Recherche Scientifique - FNRS under Grants n° : J.0179.18, J.0129.20 and IISN convention n° 4.4504.10.

DATA AVAILABILITY

The data that support the findings of this study are available from the corresponding author upon reasonable request.

[1] H. H. Funke, B. L. Grissom, C. E. McGrew, and M. W. Raynor, "Techniques for the measurement of trace moisture in high-purity electronic specialty gases," Review of scientific instruments **74**, 3909–3933 (2003).
[2] J. Burkart, D. Romanini, and S. Kassi, "Optical feedback frequency stabilized cavity ring-down spectroscopy," Optics letters **39**, 4695–4698 (2014).
[3] A. Foltynowicz, T. Ban, P. Masłowski, F. Adler, and J. Ye, "Quantum-noise-limited optical frequency comb spectroscopy," Physical review letters **107**, 233002 (2011).
[4] M. A. D. Sumner and J. Brault, *Fourier transform spectrometry* (Academic Press, 2001).
[5] P. Fellgett, *Theory of infra-red sensitivites and its application to investigations of stellar radiation in the near infra-red*, Ph.D. thesis, University of Cambridge (1951).
[6] P. Jacquinot, "17e Congres du GAMS," (1954).
[7] J. Connes and P. Connes, "Near-infrared planetary spectra by Fourier spectroscopy. I. Instruments and results," JOSA **56**, 896–910 (1966).
[8] P. R. Griffiths, "The early days of commercial FT-IR spectrometry: a personal perspective," Applied spectroscopy **71**, 329–340 (2017).
[9] A. A. Ruth, J. Orphal, and S. E. Fiedler, "Fourier-transform cavity-enhanced absorption spectroscopy using an incoherent broadband light source," Applied optics **46**, 3611–3616 (2007).
[10] T. Gherman and D. Romanini, "Mode–locked cavity–enhanced absorption spectroscopy," Optics Express **10**, 1033–1042 (2002).
[11] W. Denzer, G. Hancock, M. Islam, C. Langley, R. Peverall, G. A. Ritchie, and D. Taylor, "Trace species detection in the near infrared using Fourier transform broadband cavity enhanced absorption spectroscopy: initial studies on potential breath analytes," Analyst **136**, 801–806 (2011).
[12] D. M. O'Leary, A. A. Ruth, S. Dixneuf, J. Orphal, and R. Varma, "The near infrared cavity-enhanced absorption spectrum of methyl cyanide," Journal of Quantitative Spectroscopy and Radiative Transfer **113**, 1138–1147 (2012).
[13] J. Mandon, G. Guelachvili, and N. Picqué, "Fourier transform spectroscopy with a laser frequency comb," Nature Photonics **3**, 99–102 (2009).
[14] P. Maslowski, K. F. Lee, A. C. Johansson, A. Khodabakhsh, G. Kowzan, L. Rutkowski, A. A. Mills, C. Mohr, J. Jiang, M. E. Fermann, *et al.*, "Surpassing the path-limited resolution of Fourier-transform spectrometry with frequency combs," Physical Review A **93**, 021802 (2016).
[15] L. Rutkowski, P. Masłowski, A. Johansson, A. Khodabakhsh, and A. Foltynowicz, "Optical frequency comb Fourier transform spectroscopy with sub-nominal resolution-principles and implementation," Journal of Quantitative Spectroscopy and Radiative Transfer (2017).
[16] K. C. Cossel, *Techniques in molecular spectroscopy : from broad bandwidth to high resolution*, Ph.D. thesis, California Institute of Technology (2014).
[17] B. Guislain, R. Harvey, D. Tokaryk, A. Ross, P. Crozet, and A. Adam, "An alternative approach to interferogram collection and processing for a vintage Bomem DA3 Fourier transform spectrometer," Journal of Molecular Spectroscopy , 111181 (2019).
[18] P. Griffiths and J. De Haseth, *Fourier transform infrared spectrometry*, Vol. 171 (John Wiley & Sons, 2007).
[19] A. Libert, *Design of a Fourier transform spectrometer for high resolution spectroscopy*, Master's thesis, Universite catholique de Louvain (2016).
[20] A. Foltynowicz, P. Masłowski, T. Ban, F. Adler, K. Cossel, T. Briles, and J. Ye, "Optical frequency comb spectroscopy," Faraday discussions **150**, 23–31 (2011).
[21] A. Foltynowicz, P. Masłowski, A. J. Fleisher, B. J. Bjork, and J. Ye, "Cavity-enhanced optical frequency comb spectroscopy in the mid-infrared

application to trace detection of hydrogen peroxide," Applied Physics B **110**, 163–175 (2013).
[22]Y. Zhao, *Implementing thermal feedback control of a helium-neon laser for frequency stabilization*, Master's thesis, Ward Melville High School, East Setauket, NY (2008).
[23]"Frequency stabilization of internal-mirror helium–neon lasers, author=Balhorn, R and Kunzmann, H and Lebowsky, F," Applied optics **11**, 742–744 (1972).
[24]H. Shirvani-Mahdavi and Y. Narges, "Frequency stabilization of ambience-isolated internal-mirror He–Ne lasers by thermoelectric-cooling thermal compensation," Journal of Theoretical and Applied Physics **10**, 315–321 (2016).
[25]L. Comolli and B. Saggin, "Analysis of disturbances in the Planetary Fourier Spectrometer through numerical modeling," Planetary and Space science **58**, 864–874 (2010).
[26]C. A. Michaels, T. Masiello, and P. M. Chu, "Fourier transform spectrometry with a near-infrared supercontinuum source," Applied spectroscopy **63**, 538–543 (2009).
[27]V. V. Goncharov and G. E. Hall, "Supercontinuum Fourier transform spectrometry with balanced detection on a single photodiode," The Journal of chemical physics **145**, 084201 (2016).
[28]P. C. Hobbs, "Ultrasensitive laser measurements without tears," Applied optics **36**, 903–920 (1997).
[29]J. L. Hall, M. S. Taubman, and J. Ye, "Laser stabilization," in *Handbook of Optics IV*, edited by J. M. Enoch, E. V. Stryland, and W. L. Wolves (McGraw-Hill, New York, Washington D.C., 2000) Chap. 27.
[30]H. Yang, P. R. Griffiths, and C. J. Manning, "Improved data processing by application of Brault's method to ultra-rapid-scan FT-IR spectrometry," Applied spectroscopy **56**, 1281–1288 (2002).
[31]D. A. Naylor, T. R. Fulton, P. W. Davis, I. M. Chapman, B. G. Gom, L. D. Spencer, J. V. Lindner, N. E. Nelson-Fitzpatrick, M. K. Tahic, and G. R. Davis, "Data processing pipeline for a time-sampled imaging Fourier transform spectrometer," in *Imaging Spectrometry X*, Vol. 5546 (International Society for Optics and Photonics, 2004) pp. 61–72.
[32]W. Herres and J. Gronholz, "Understanding FT-IR data processing," Part **1**, 352–356 (1984).
[33]S. Haykin and B. V. Veen, *Signals and systems* (John Wiley & Sons, 2007).
[34]D. A. Naylor and M. K. Tahic, "Apodizing functions for Fourier transform spectroscopy," JOSA A **24**, 3644–3648 (2007).
[35]J. W. Brault, "High precision fourier transform spectrometry: The critical role of phase corrections," Microchimica Acta **93**, 215–227 (1987).
[36]L. Mertz, "Auxiliary computation for Fourier spectrometry," Infrared Physics **7**, 17–23 (1967).
[37]M. L. Forman, W. H. Steel, and G. A. Vanasse, "Correction of asymmetric interferograms obtained in Fourier spectroscopy," JOSA **56**, 59–63 (1966).
[38]J. W. Brault, "New approach to high-precision Fourier transform spectrometer design," Applied Optics **35**, 2891–2896 (1996).
[39]L. S. Rothman, I. E. Gordon, A. Barbe, D. C. Benner, P. F. Bernath, M. Birk, V. Boudon, L. R. Brown, A. Campargue, J.-P. Champion, *et al.*, "The HITRAN 2008 molecular spectroscopic database," Journal of Quantitative Spectroscopy and Radiative Transfer **110**, 533–572 (2009).
[40]J. C. Cobas, M. A. Bernstein, M. Martín-Pastor, and P. G. Tahoces, "A new general-purpose fully automatic baseline-correction procedure for 1D and 2D NMR data," Journal of Magnetic Resonance **183**, 145–151 (2006).
[41]R. Learner, A. Thorne, and J. W. Brault, "Ghosts and artifacts in Fourier-transform spectrometry," Applied optics **35**, 2947–2954 (1996).
[42]M. L. Salit, J. C. Travis, and M. R. Winchester, "Practical wavelength calibration considerations for UV–visible Fourier-transform spectroscopy," Applied optics **35**, 2960–2970 (1996).
[43]M. L. Salit, C. J. Sansonetti, D. Veza, and J. C. Travis, "Investigation of single-factor calibration of the wave-number scale in fourier-transform spectroscopy," JOSA B **21**, 1543–1550 (2004).
[44]R. Hawkins, M. Hoke, and J. Shaw, "Wavenumber calibration of Fourier transform spectra," Applied Spectroscopy **37**, 134–139 (1983).
[45]S. E. Fiedler, A. Hese, and A. A. Ruth, "Incoherent broad-band cavity-enhanced absorption spectroscopy," Chemical physics letters **371**, 284–294 (2003).
[46]P. Masłowski, K. Cossel, A. Foltynowicz, and J. Ye, "Cavity-enhanced direct frequency comb spectroscopy," in *Cavity-Enhanced Spectroscopy and Sensing* (Springer, 2014) pp. 271–321.

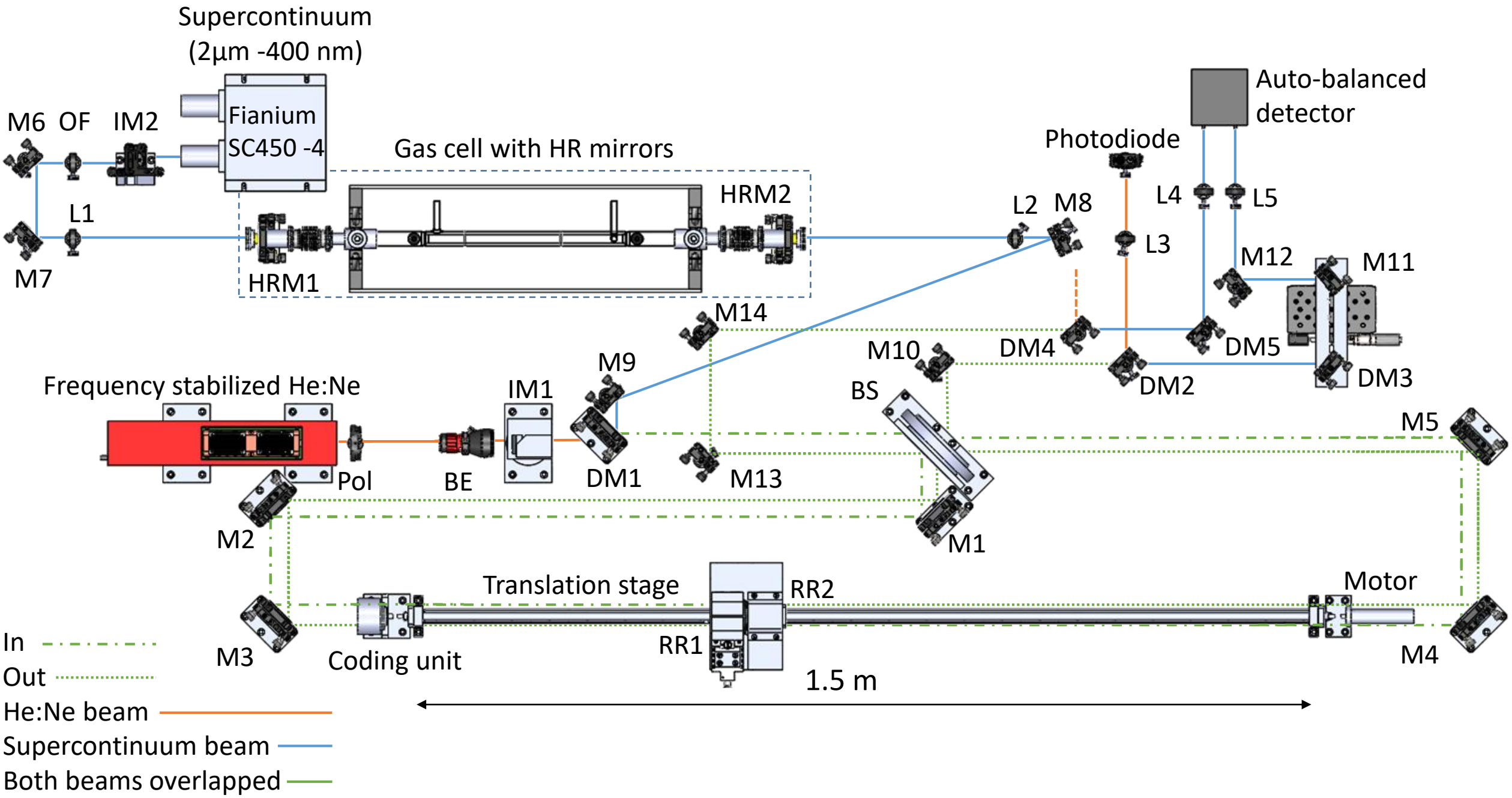
Supercontinuum
(2µm -400 nm)
Fianium
SC450 -4
M6
OF
IM2
L1
M7
Gas cell with HR mirrors
HRM1
HRM2
Auto-balanced
detector
Photodiode
L2
M8
L3
L4
L5
M12
M11
DM4
DM5
DM2
DM3
M14
M10
M9
IM1
BS
M5
Frequency stabilized He:Ne
Pol
BE
DM1
M13
M2
M1
Translation stage
RR2
Motor
M3
Coding unit
RR1
M4
1.5 m
In
Out
He:Ne beam
Supercontinuum beam
Both beams overlapped

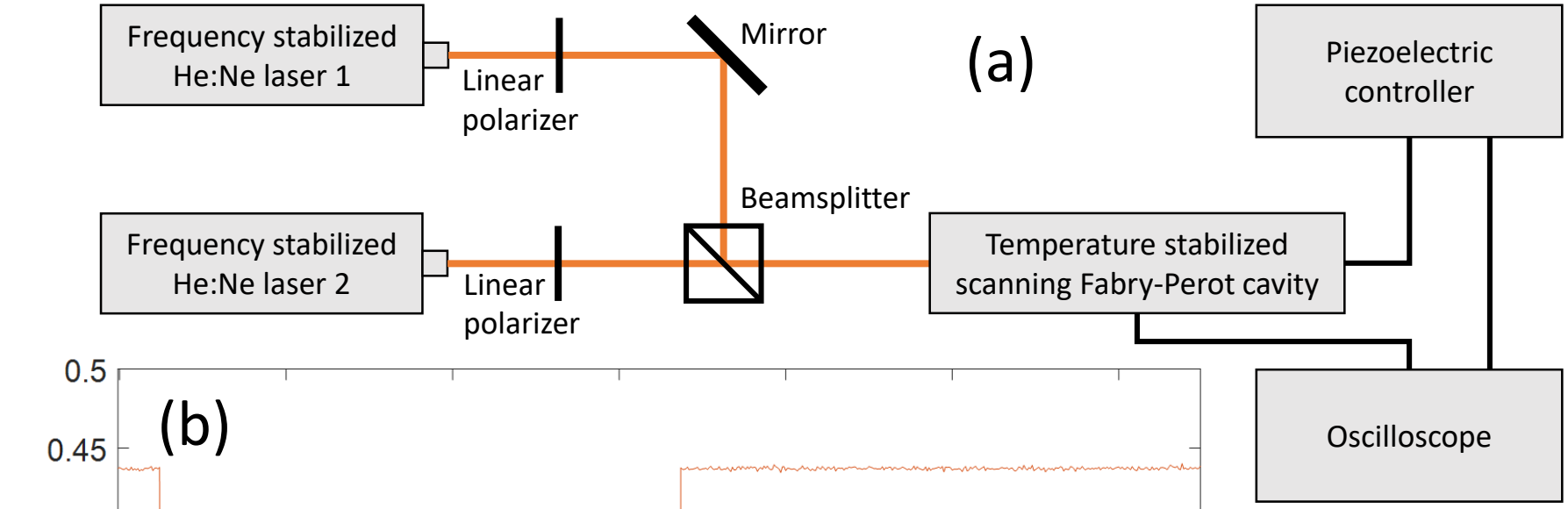
Frequency stabilized
He:Ne laser 1
Linear
polarizer
Mirror
Beamsplitter
Frequency stabilized
He:Ne laser 2
Linear
polarizer
Temperature stabilized
scanning Fabry-Perot cavity
Piezoelectric
controller
Oscilloscope

(a)

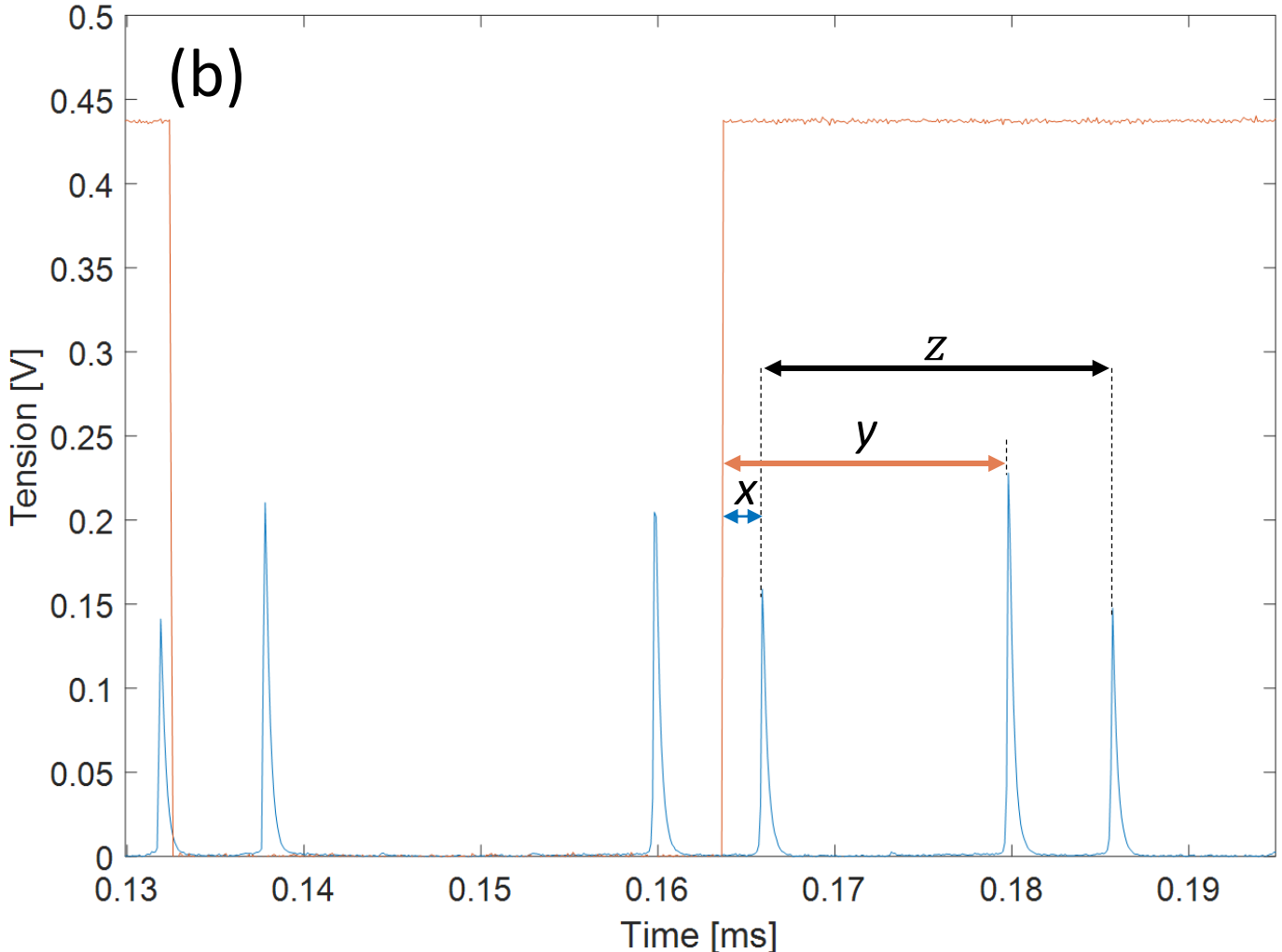
(b)
Tension [V]
Time [ms]
z
y
x
0.5
0.45
0.4
0.35
0.3
0.25
0.2
0.15
0.1
0.05
0
0.13
0.14
0.15
0.16
0.17
0.18
0.19

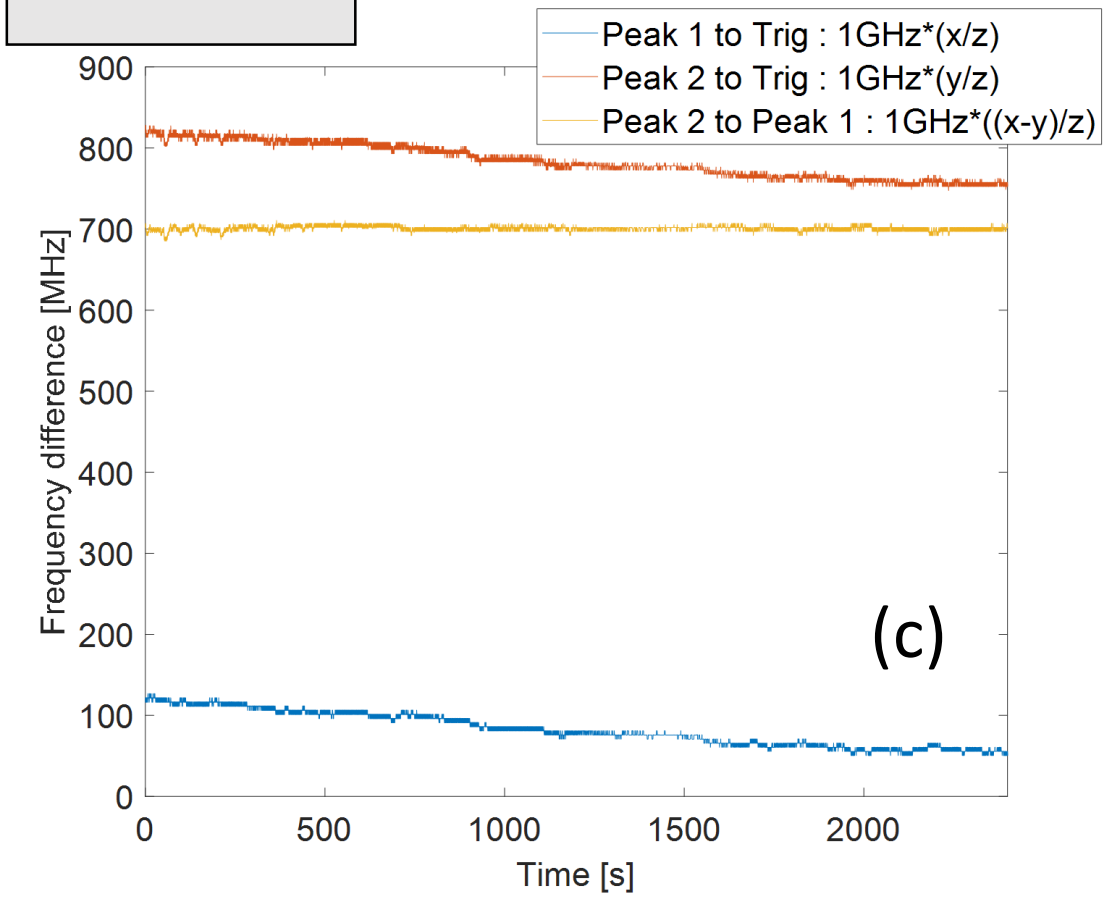
Peak 1 to Trig : 1GHz*(x/z)
Peak 2 to Trig : 1GHz*(y/z)
Peak 2 to Peak 1 : 1GHz*((x-y)/z)
Frequency difference [MHz]
Time [s]
(c)
900
800
700
600
500
400
300
200
100
0
0
500
1000
1500
2000

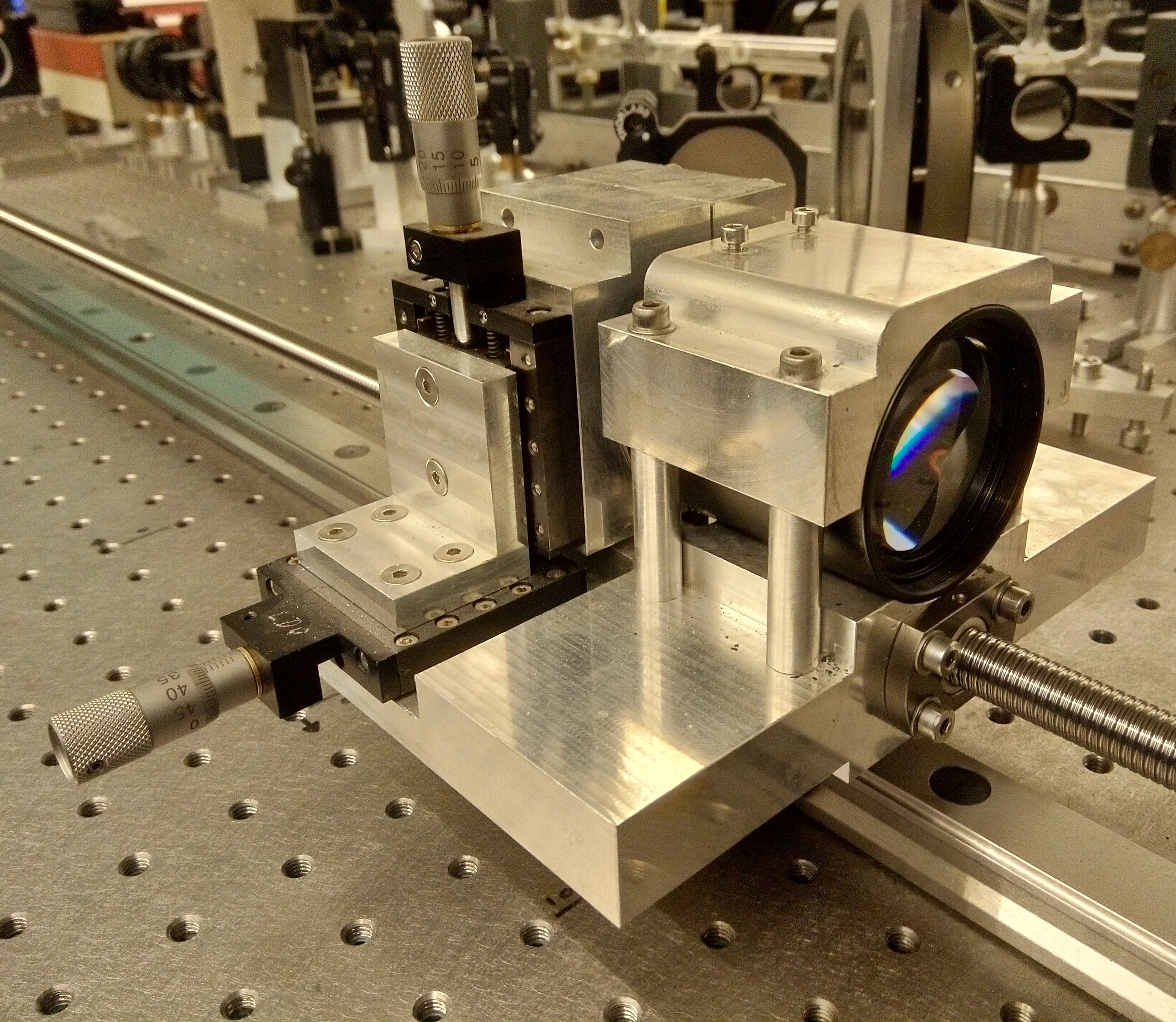

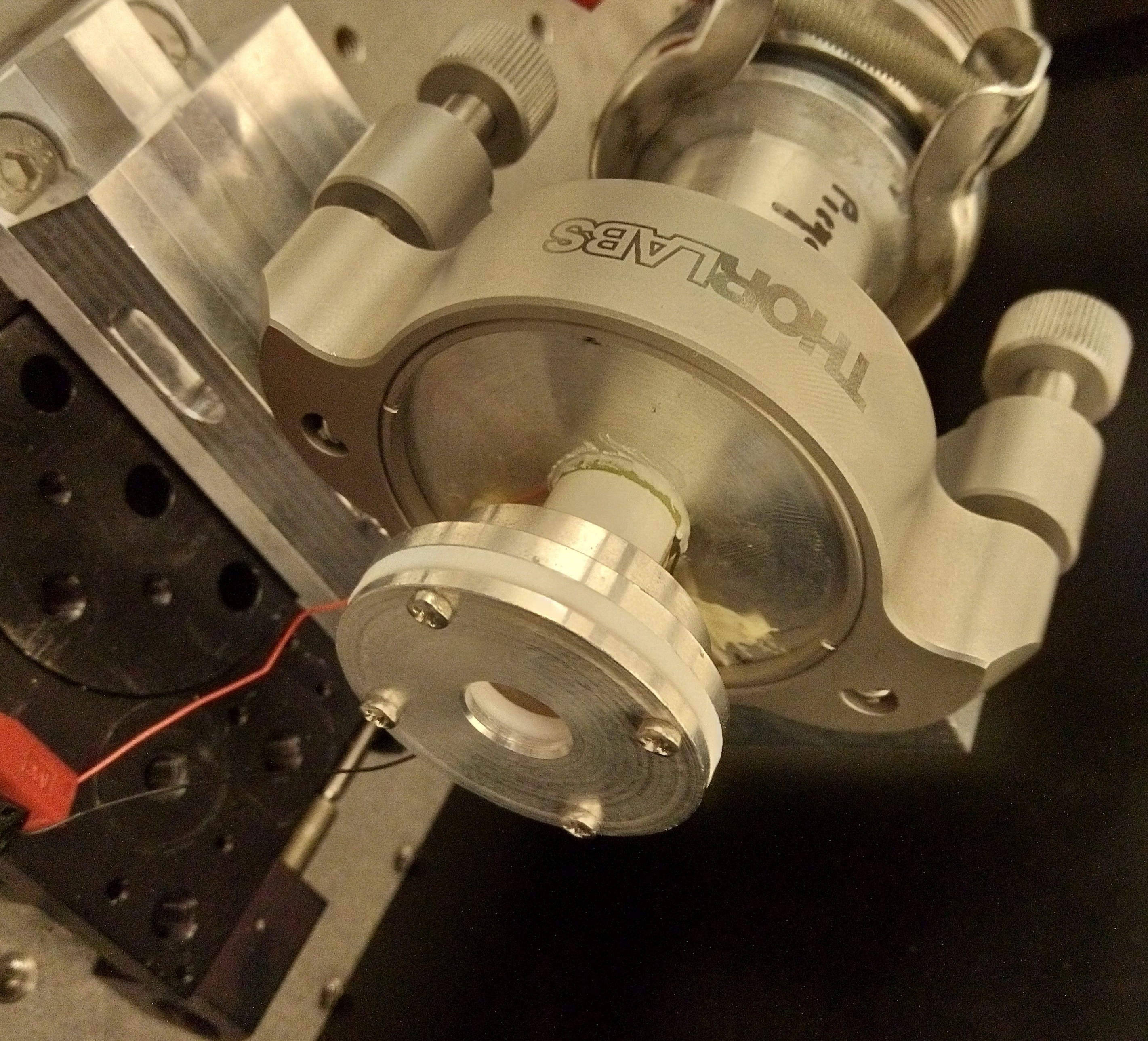
THORLABS

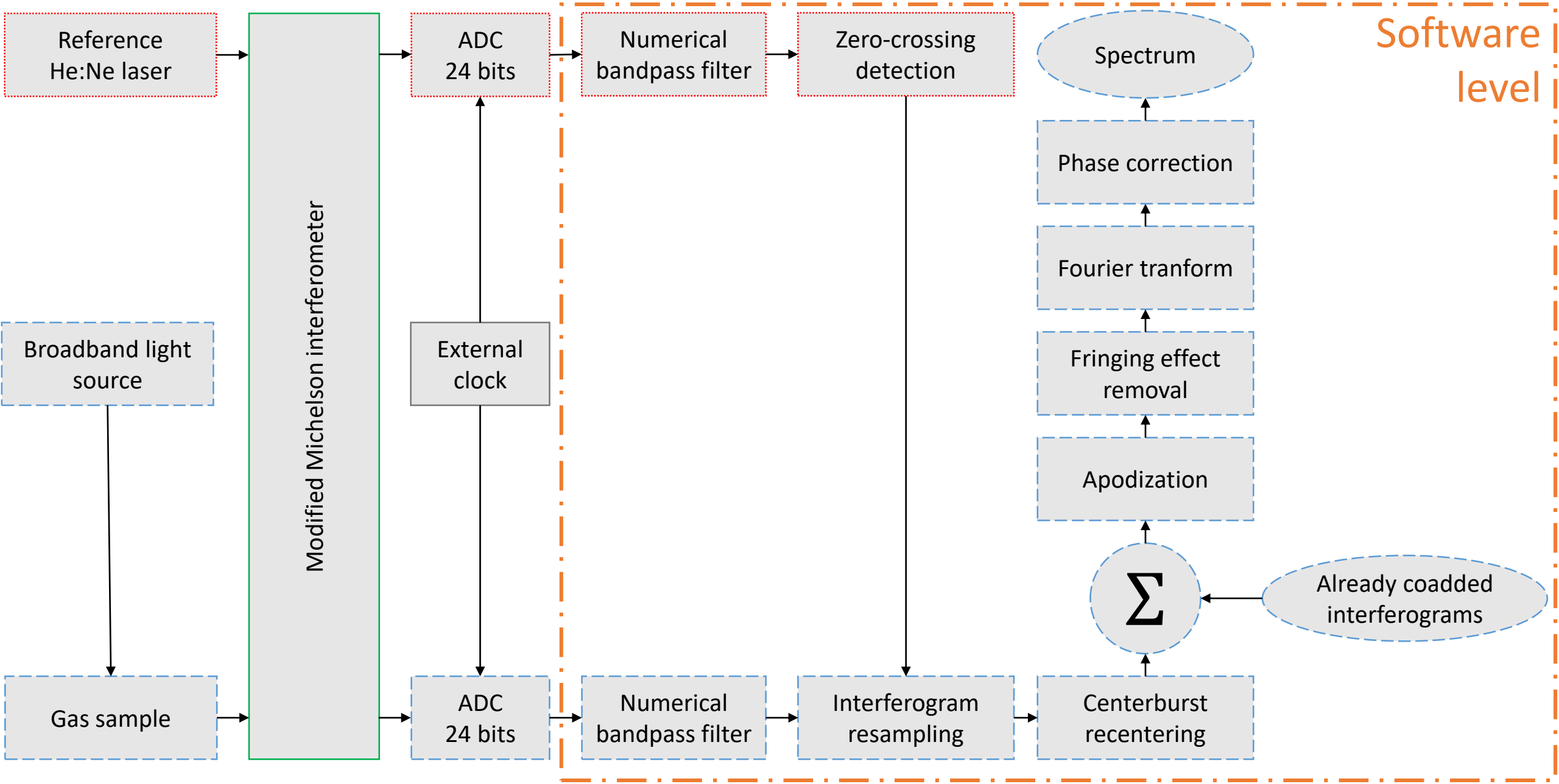
Reference
He:Ne laser
Modified Michelson interferometer
ADC
24 bits
Numerical
bandpass filter
Zero-crossing
detection
Spectrum
Phase correction
Fourier tranform
Fringing effect
removal
Apodization
Σ
Already coadded
interferograms
Software
level
Broadband light
source
External
clock
Gas sample
ADC
24 bits
Numerical
bandpass filter
Interferogram
resampling
Centerburst
recentering

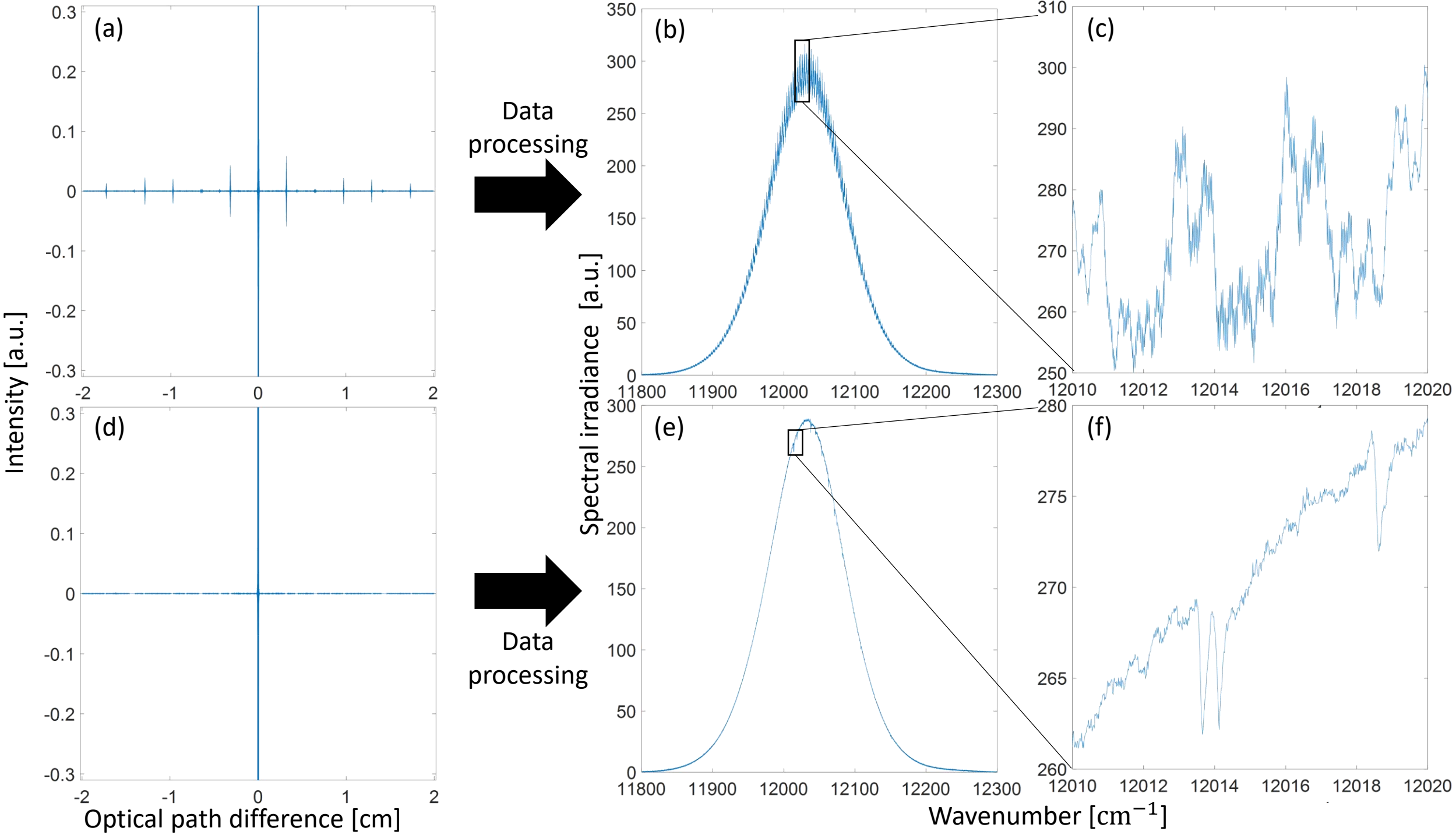
(a)
(b)
(c)
(d)
(e)
(f)
Data processing
Data processing
Intensity [a.u.]
Spectral irradiance [a.u.]
Optical path difference [cm]
Wavenumber [cm^{-1}]

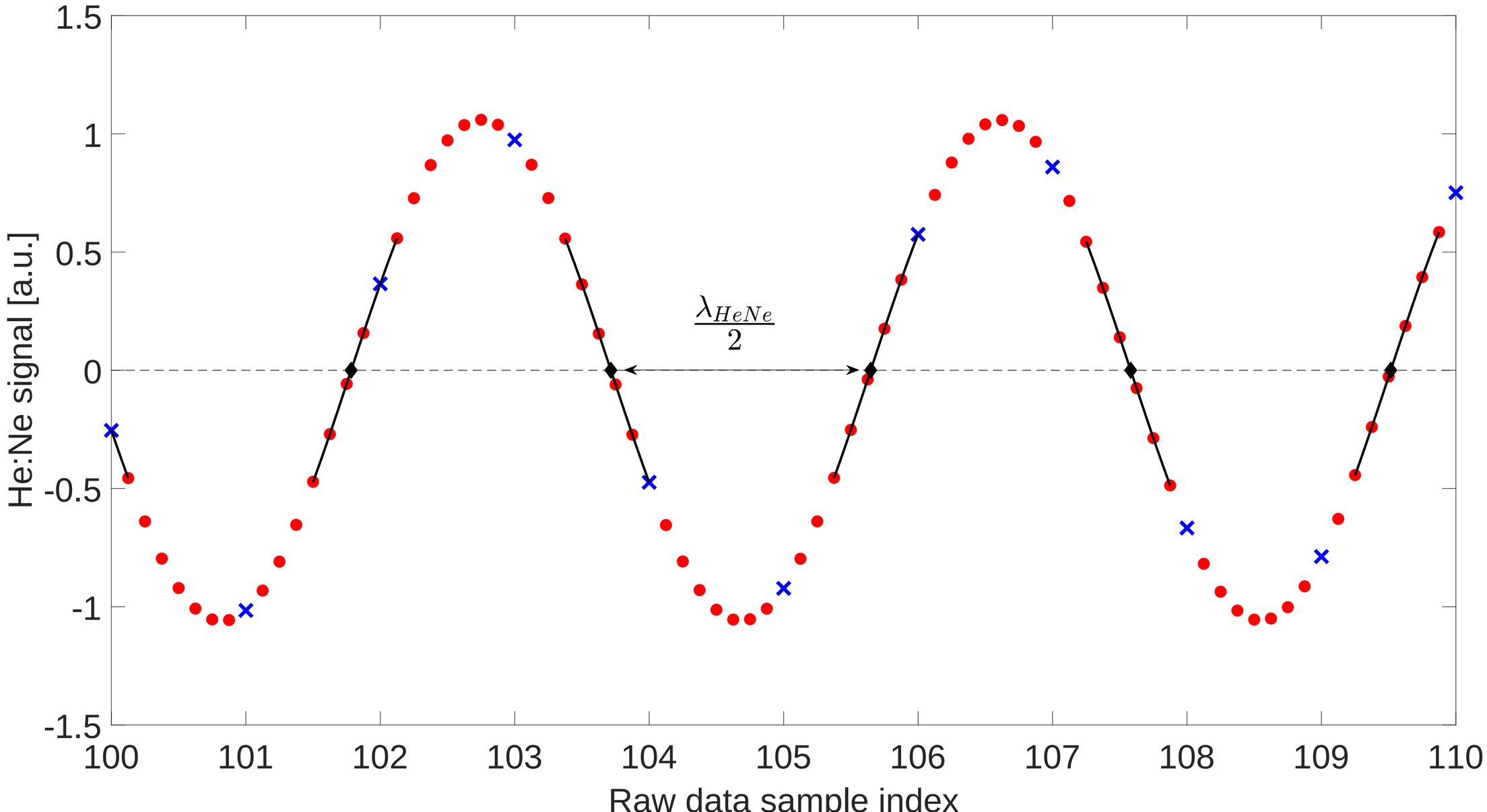
1.5
1
0.5
0
-0.5
-1
-1.5
He:Ne signal [a.u.]
100
101
102
103
104
105
106
107
108
109
110
Raw data sample index
$\frac{\lambda_{HeNe}}{2}$

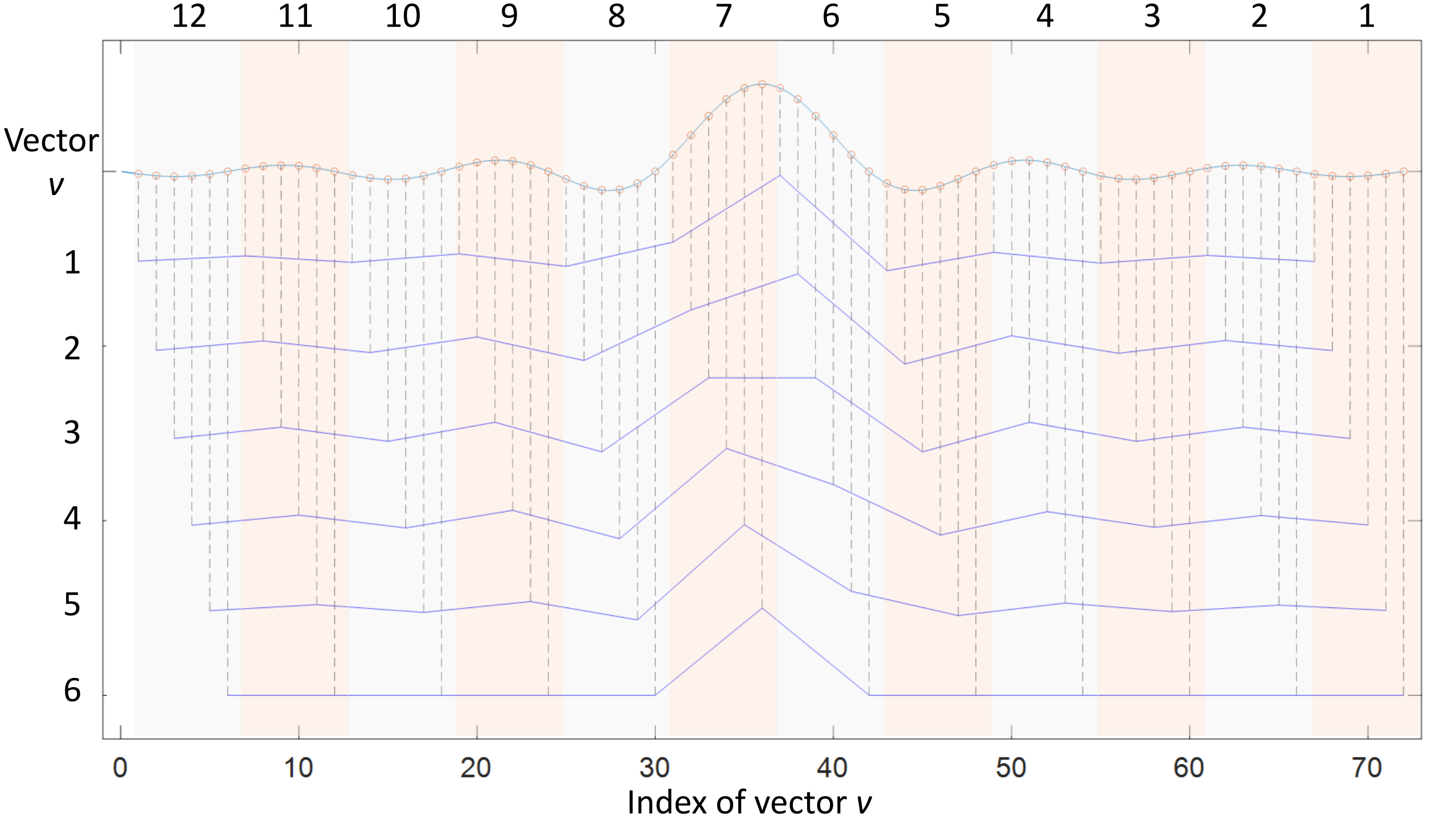
12
11
10
9
8
7
6
5
4
3
2
1
Vector
v
1
2
3
4
5
6
0
10
20
30
40
50
60
70
Index of vector v

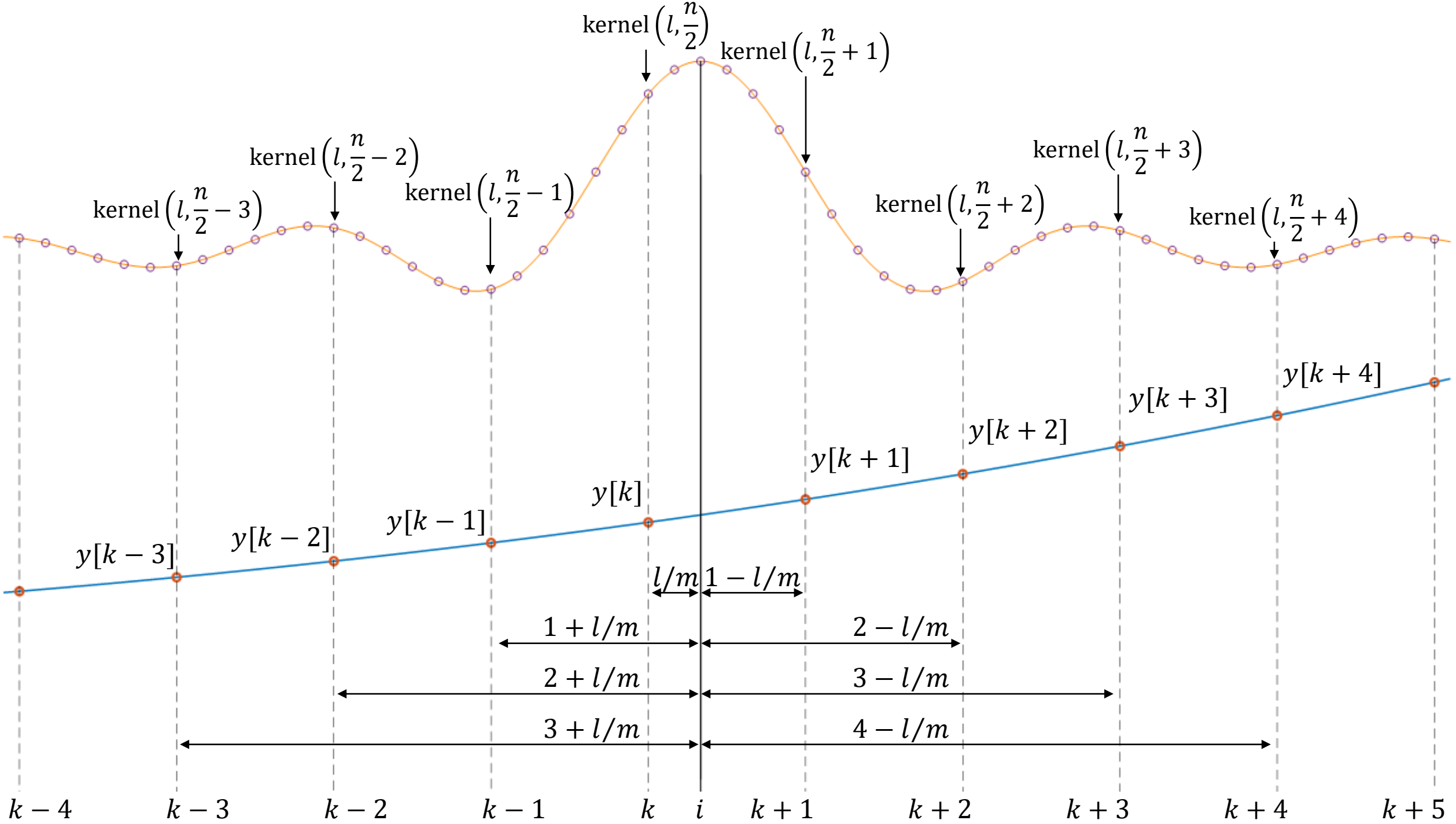
kernel $\left(l, \frac{n}{2}\right)$
kernel $\left(l, \frac{n}{2}+1\right)$
kernel $\left(l, \frac{n}{2}-2\right)$
kernel $\left(l, \frac{n}{2}-3\right)$
kernel $\left(l, \frac{n}{2}-1\right)$
kernel $\left(l, \frac{n}{2}+2\right)$
kernel $\left(l, \frac{n}{2}+3\right)$
kernel $\left(l, \frac{n}{2}+4\right)$
$y[k-3]$
$y[k-2]$
$y[k-1]$
$y[k]$
$y[k+1]$
$y[k+2]$
$y[k+3]$
$y[k+4]$
l/m
$1-l/m$
$1+l/m$
$2-l/m$
$2+l/m$
$3-l/m$
$3+l/m$
$4-l/m$
$k-4$
$k-3$
$k-2$
$k-1$
k
i
$k+1$
$k+2$
$k+3$
$k+4$
$k+5$

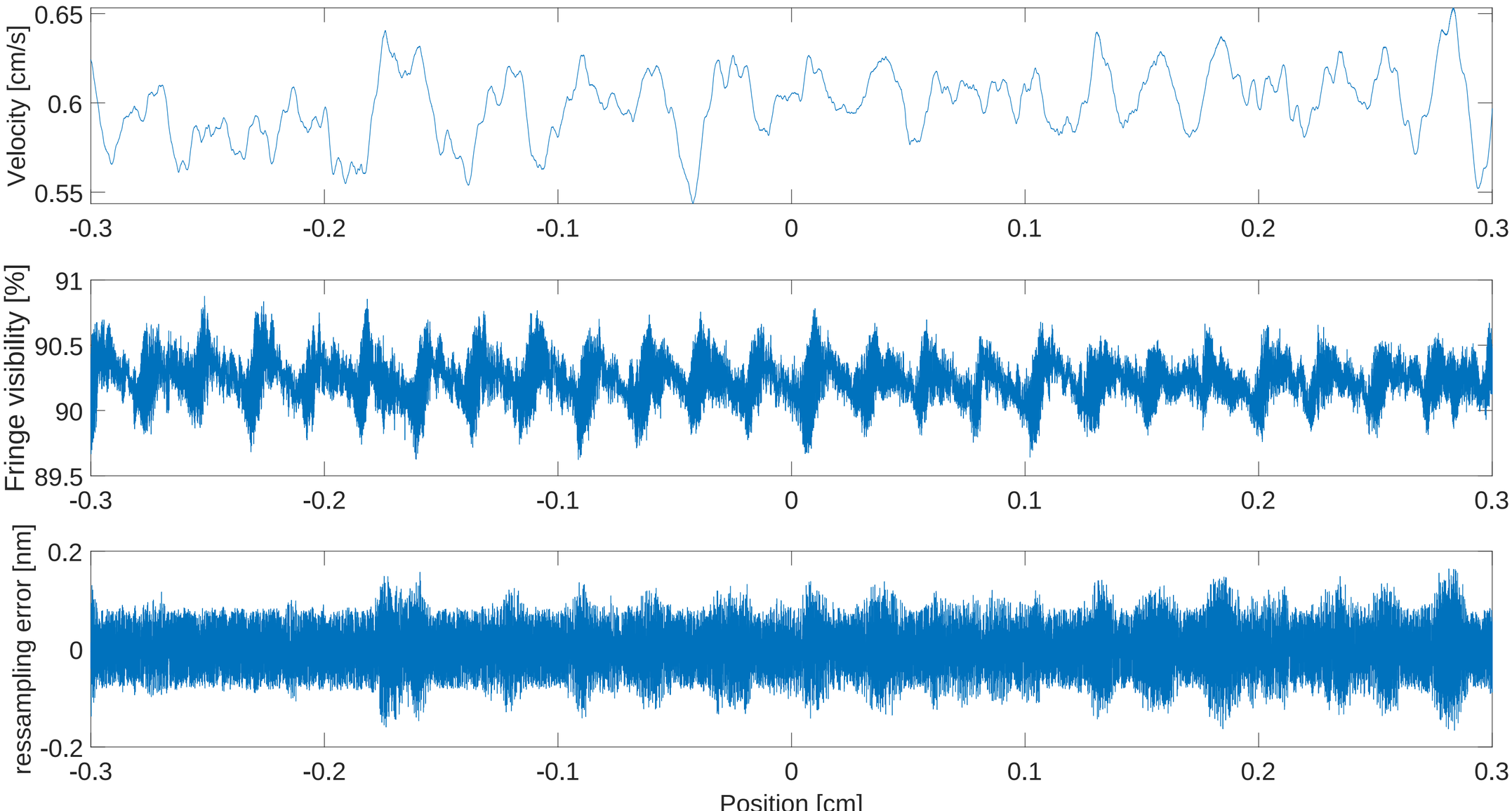
Velocity [cm/s]
0.65
0.6
0.55
Fringe visibility [%]
91
90.5
90
89.5
ressampling error [nm]
0.2
0
-0.2
-0.3
-0.2
-0.1
0
0.1
0.2
0.3
Position [cm]

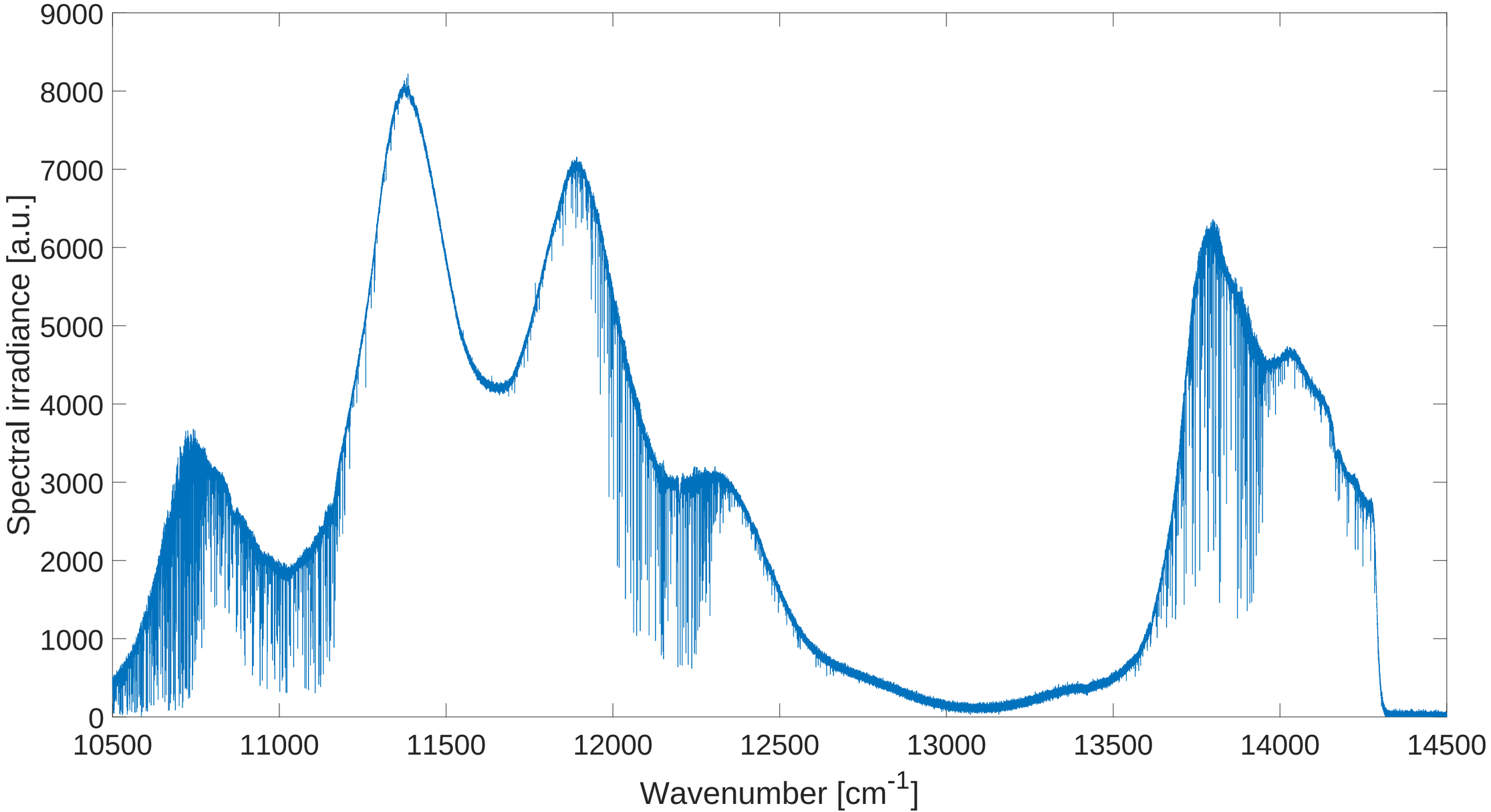
Spectral irradiance [a.u.]
9000
8000
7000
6000
5000
4000
3000
2000
1000
0
10500
11000
11500
12000
12500
13000
13500
14000
14500
Wavenumber [cm-1]

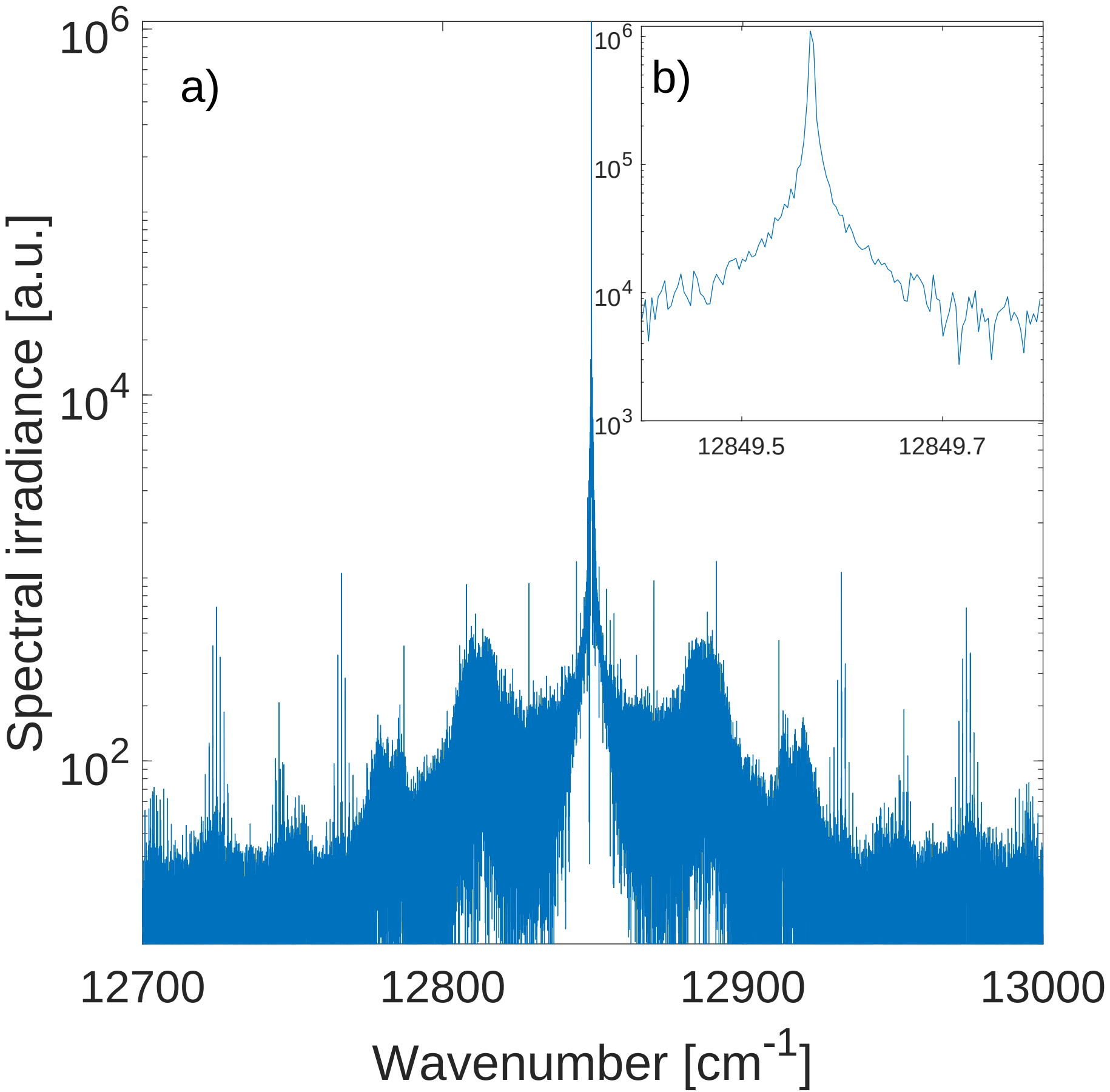
a)
b)
10^6
10^4
10^2
10^5
10^3
12849.5
12849.7
Spectral irradiance [a.u.]
12700
12800
12900
13000
Wavenumber [cm^{-1}]

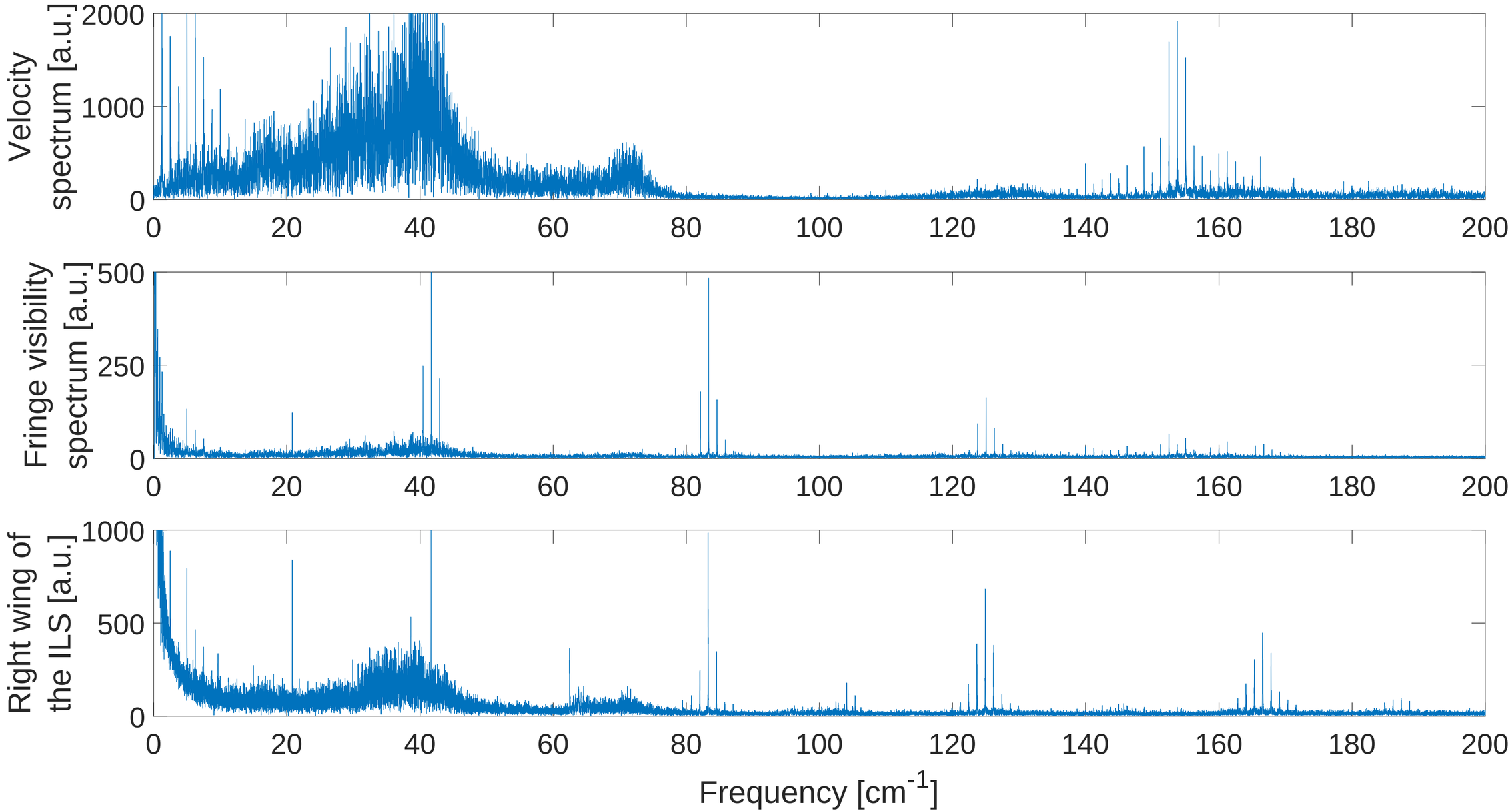
Velocity spectrum [a.u.]
2000
1000
0
Fringe visibility spectrum [a.u.]
500
250
0
Right wing of the ILS [a.u.]
1000
500
0
0
20
40
60
80
100
120
140
160
180
200
Frequency [cm-1]

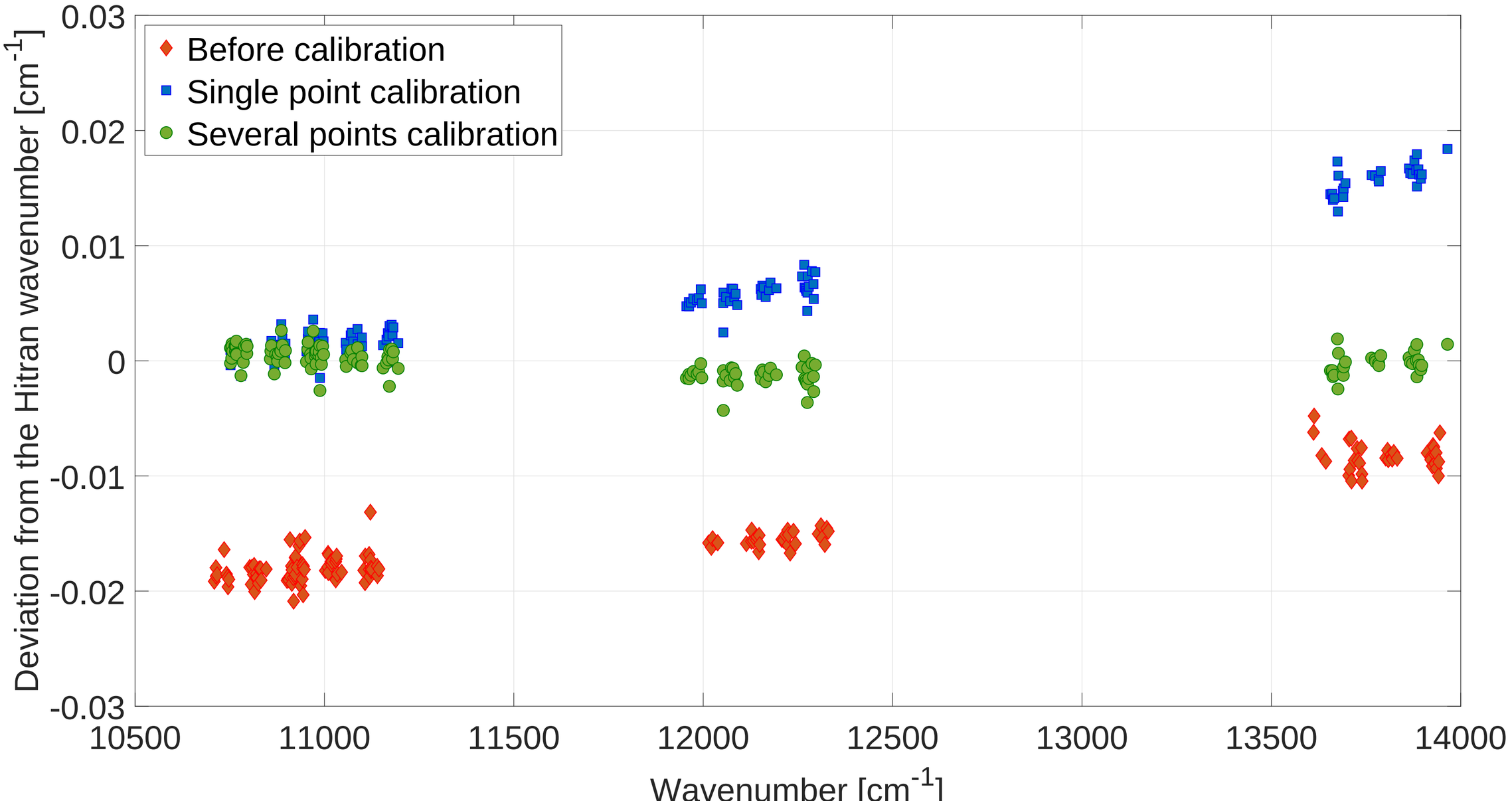
Before calibration
Single point calibration
Several points calibration
Deviation from the Hitran wavenumber [cm-1]
Wavenumber [cm-1]
0.03
0.02
0.01
0
-0.01
-0.02
-0.03
10500
11000
11500
12000
12500
13000
13500
14000

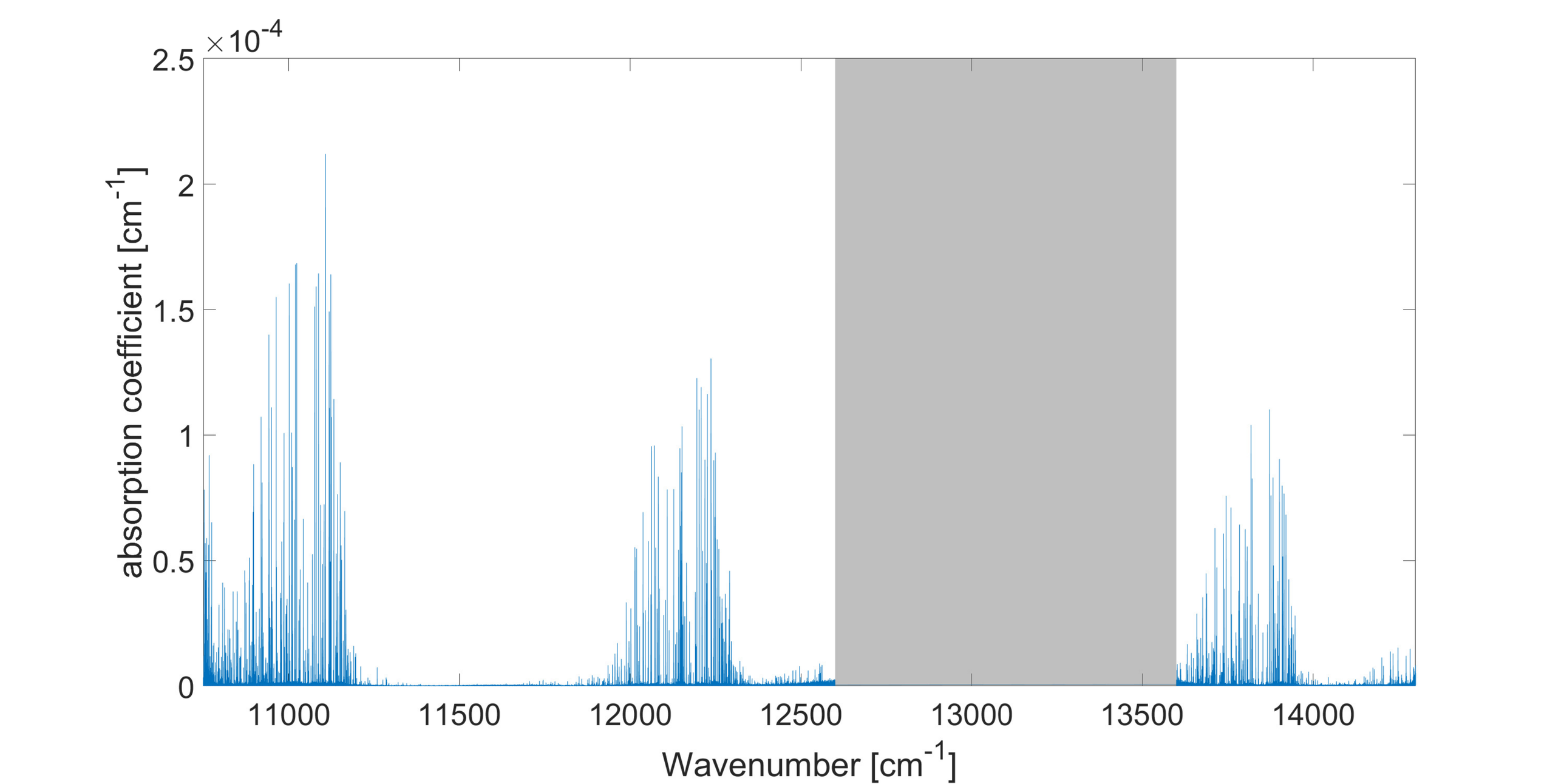
×10^-4
2.5
2
1.5
1
0.5
0
absorption coefficient [cm^-1]
11000
11500
12000
12500
13000
13500
14000
Wavenumber [cm^-1]

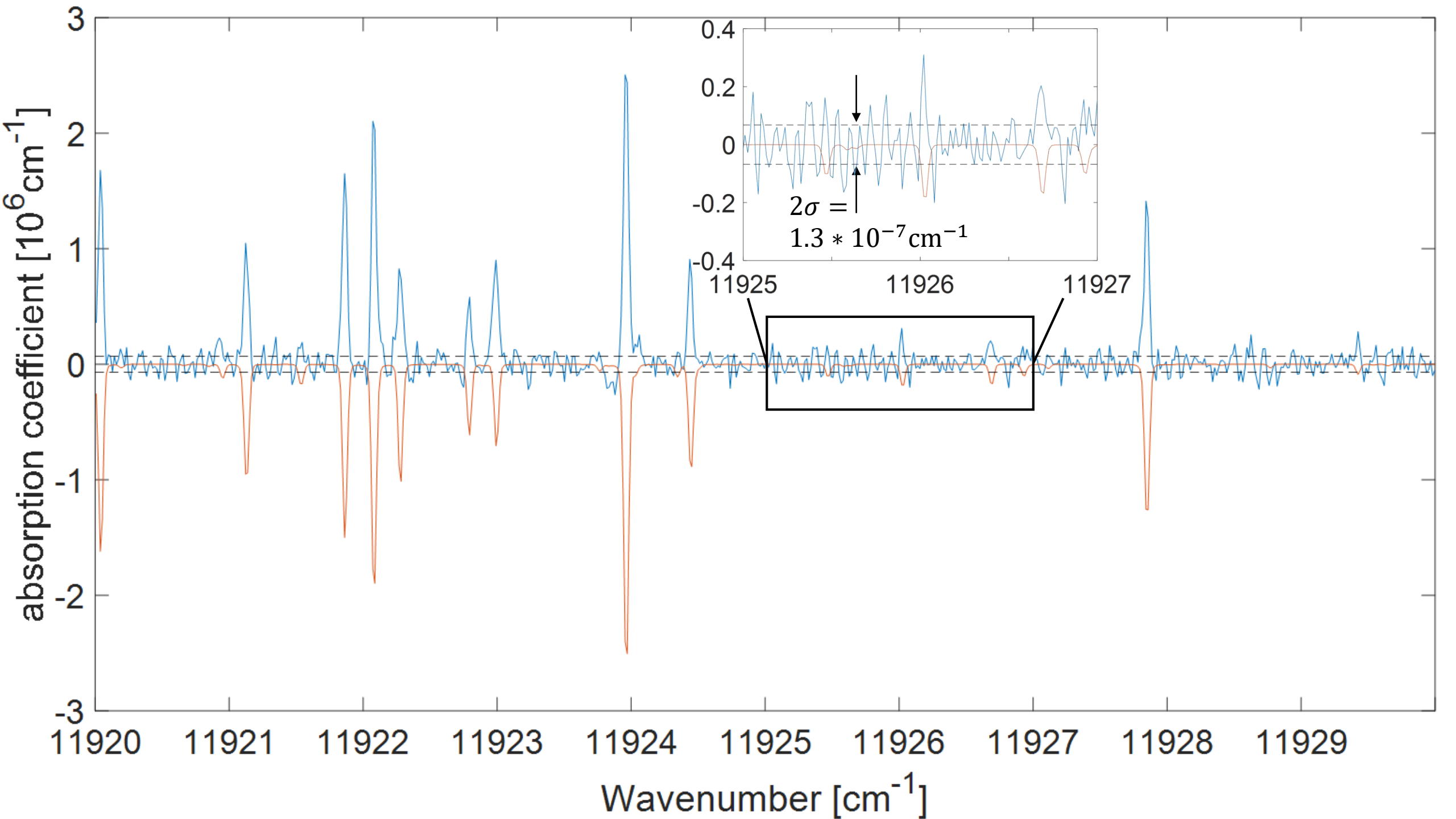
absorption coefficient [10^6 cm^-1]
Wavenumber [cm^-1]
3
2
1
0
-1
-2
-3
11920
11921
11922
11923
11924
11925
11926
11927
11928
11929
0.4
0.2
0
-0.2
-0.4
11925
11926
11927
2σ =
1.3 ∗ 10^−7 cm^−1